Received: 8 June 2020 | Revised: 30 October 2020 | Accepted: 13 December 2020

DOI: 10.1002/nag.3183

RESEARCH ARTICLE

WILEY

Noncoaxiality considering inherent anisotropy under various loading paths in a strain space multiple mechanism model for granular materials

Kyohei Ueda[1] | **Susumu Iai**[2]

[1] Disaster Prevention Research Institute, Kyoto University, Gokasho, Uji, Kyoto, Japan

[2] FLIP Consortium, Nakagyo-ku, Kyoto, Japan

Correspondence
Kyohei Ueda, Disaster Prevention Research Institute, Kyoto University, Gokasho, Uji, Kyoto 611-0011, Japan.
Email: ueda.kyohei.2v@kyoto-u.ac.jp

Abstract

Inherent anisotropy is a crucial aspect to consider to improve one's understanding of the behavior of granular materials, in particular, noncoaxial responses under proportional and nonproportional loadings. This article investigates the capability of a strain space multiple mechanism model to reproduce complex responses of inherently anisotropic soils under various loading paths. The constitutive model has been expanded upon to account for the effect of inherent anisotropy by incorporating a new function along with three additional parameters; two of these parameters, a_1 and a_2, control the degree of anisotropy, whereas the third parameter, θ_0, represents the principal direction of inherent anisotropy. Laboratory experimental data regarding the complex anisotropic responses of Toyoura sand under various loading paths are used to validate the constitutive model. The model is found to successfully simulate the anisotropic drained soil responses under monotonic proportional and nonproportional loadings as well as those under loading involving the rotation of the principal stress axis by considering the additional anisotropic parameters. Furthermore, the simulated responses of inherently isotropic materials are compared with those of anisotropic materials to numerically investigate the influence of inherent anisotropy (ie, the anisotropic parameters) on soil behavior under such loading conditions.

KEYWORDS

constitutive model, granular material, inherent anisotropy, noncoaxiality, principal stress rotation

1 | INTRODUCTION

Noncoaxiality between the principal directions of stress and strain increment is a crucial aspect to consider for the development of constitutive models of granular materials. Experimental methods have vigorously investigated the noncoaxial behaviors of geomaterials caused by stress-induced anisotropy since the mid-1980s; Miura et al,[1] Pradel et al,[2] and Gutierrez et al[3,4] perform hollow cylinder torsional shear tests on Toyoura sand to study the noncoaxial behavior subject to proportional monotonic loading and the rotation of the principal stress axis. In a two-dimensional stress state shown in

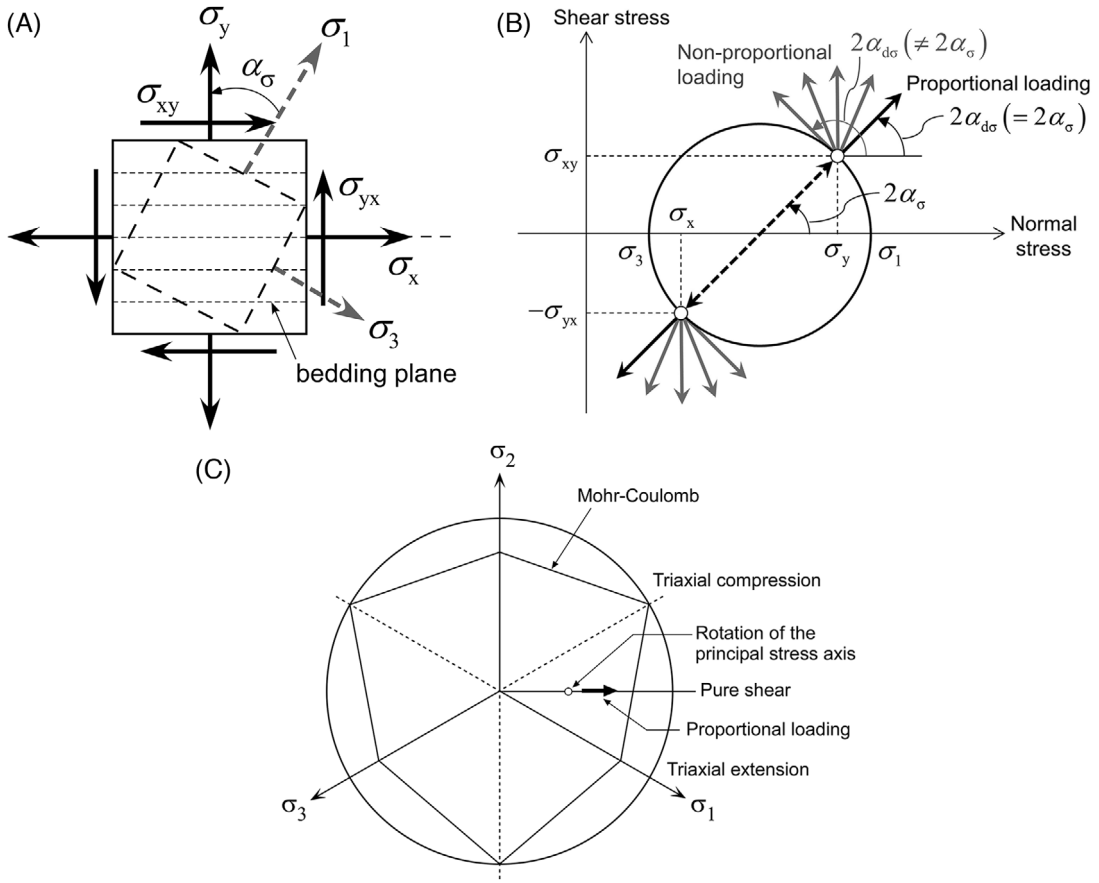

FIGURE 1 (A) Two-dimensional stress state; (B) proportional and nonproportional loading in two-dimensional Mohr's circle; (C) proportional loading and rotation of the principal stress axis in the deviatoric (or π-) plane

Figure 1A, the major principal stress direction, α_σ, can be visually captured through a two-dimensional Mohr's circle, as shown in Figure 1B. During the proportional loading, the stress increments, of which principal direction, $\alpha_{d\sigma}$, is identical with the current principal stress direction (ie, $\alpha_{d\sigma} = \alpha_\sigma$); thus, the noncoaxial behavior of the stress increments and associated strain increments, of which principal direction is given as $\alpha_{d\varepsilon}$, is possible to investigate simply as the noncoaxiality between $\alpha_{d\varepsilon}$ and α_σ. Meanwhile, the rotation of the principal stress axis can be categorized into nonproportional loading (ie, $\alpha_{d\sigma} \neq \alpha_\sigma$) shown in Figure 1B; in this case, the (incremental) noncoaxiality between $\alpha_{d\sigma}$ and $\alpha_{d\varepsilon}$ is also defined, besides the noncoaxiality between α_σ and $\alpha_{d\varepsilon}$. It should be noted that the two-dimensional analyses in this study correspond to the pure shear in the deviatoric (or π–) plane, as shown in Figure 1C; the proportional loading in Figure 1B is represented by the arrow, while the rotation of the principal stress axis is represented by a single fixed point in the plane because the three principal stresses (ie, σ_1, σ_2, and σ_3) are all invariant (ie, keeping constant values) during the rotation of the principal stress axis. Since the plastic strain increment becomes dominant as the material nonlinearity becomes stronger compared to the elastic component, Gutierrez et al[3,4] investigate the principal direction of plastic strain increment, $\alpha_{d\varepsilon^p}$, by assuming $\alpha_{d\varepsilon^e}$ coaxial with $\alpha_{d\sigma}$ (that is correct unless inherent anisotropy affects the elastic shear modulus as described later in Equation 27); they conclude that the applied stress direction significantly affects $\alpha_{d\varepsilon^p}$, and the degree of noncoaxiality between α_σ and $\alpha_{d\varepsilon^p}$ decreases as the stress ratio increases.

For better understanding of the strength and deformation characteristics of granular materials, including their noncoaxial behavior, inherent anisotropy (also referred to as initial fabric anisotropy) is also essential to consider. Inherent anisotropy is thought to arise from the preferred particle arrangement and contact orientation of granular material particles during sedimentation.[5,6] The inherent anisotropy of granular materials has been a subject of intense experimental investigation using a triaxial testing apparatus[5–8] and a hollow-cylinder torsional-shear apparatus.[9–12] These experimental outcomes have been used for the validation and verification of constitutive models, which can account for the effect of inherent anisotropy[13–20]; a strain space multiple mechanism model[21–24] has also been expanded to represent the effect of inherent anisotropy, and its fundamental capability has been demonstrated.[25] A numerical

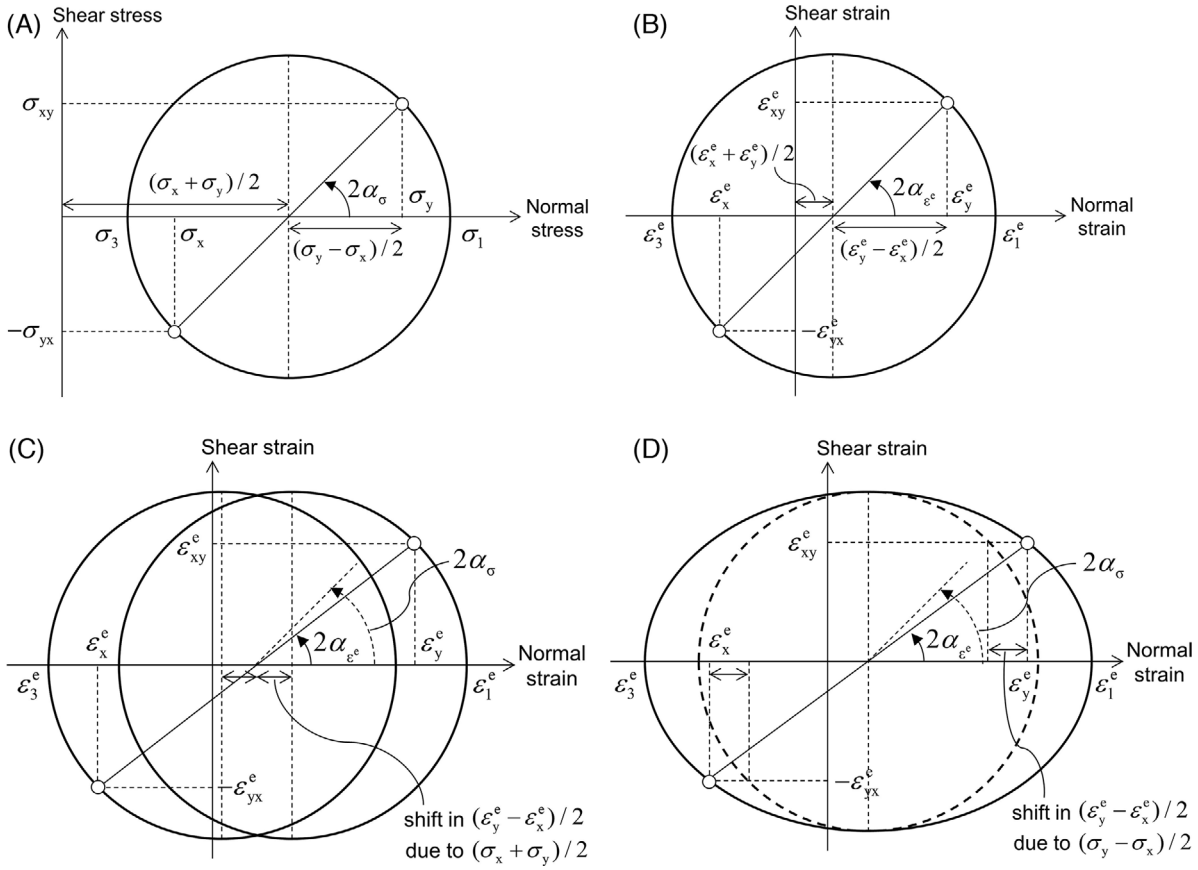

FIGURE 2 Mohr's circle for two-dimensional: (A) applied stress components; (B) strain responses in isotropic linear elastic materials; (C), (D) strain responses in orthotropic linear elastic materials

study using these constitutive models is useful to investigate the possibility that the inherent anisotropy due to the deposition process and grain characteristics of granular materials contributes to macroscopic soil responses, including noncoaxiality.[14,15,18] Two-dimensional discrete element method simulations of granular materials[26–31] also report that noncoaxiality is dependent on the material's inherent anisotropy as well as the loading history.

If we focus on the behavior in the elastic domain, the effect of inherent anisotropy on noncoaxiality can be intuitively explained as follows. First, isotropic elastic materials show the coaxial behavior between the applied stress components in Figure 2A and associated strain responses in Figure 2B (ie, $\alpha_\sigma = \alpha_{\varepsilon^e}$) because their stiffness (eg, Young's modulus) is directionally independent. However, in the case of orthogonal anisotropic elastic materials (as indicated by the bedding plane in Figure 1A), the axial responses in the x- and y-directions are considered different. When normal stresses of the same magnitude are applied in the two directions, one direction shows a hard response while the other a soft response, leading to a more significant strain in the latter direction than in the former direction. Hence, a nonzero normal strain difference, $\varepsilon^e_y - \varepsilon^e_x$, occurs even under the isotropic stress state (or under the condition of $\sigma_y - \sigma_x = 0$). When the stress difference is nonzero, as shown in Figure 2A, this change in $\varepsilon^e_y - \varepsilon^e_x$ induced by the isotropic stress complicates the (isotropic) strain circle in Figure 2B, as shown in Figure 2C. Furthermore, the different stiffness in the two directions results in much different $\varepsilon^e_y - \varepsilon^e_x$ responses to the same (nonzero) stress difference than in isotropic elastic materials; the inherent anisotropy distorts the (isotropic) strain circle in Figure 2B into that shown in Figure 2D. It is noted that this figure ignores the shift in $\varepsilon^e_y - \varepsilon^e_x$ due to the isotropic stress state for simplicity. Comparison of the anisotropic strain circles in Figures 2C and 2D with the isotropic ones demonstrates that the principal strain direction is also affected by the inherent anisotropy, resulting in noncoaxiality between the directions of principal stress and strain (ie,$\alpha_\sigma \neq \alpha_{\varepsilon^e}$). For a more theoretical explanation of orthotropic linear elastic materials,[32,33] refer to the formulas in Appendix A.

The dependency of noncoaxiality on inherent anisotropy in the nonlinear (or plastic) domain is, of course, expected to be more complicated; this is because inherent anisotropy also exerts an influence on the failure surface of soils besides the initial elastic modulus (as described later in Equation 28 and Figure 11). However, the strain space multiple mechanism

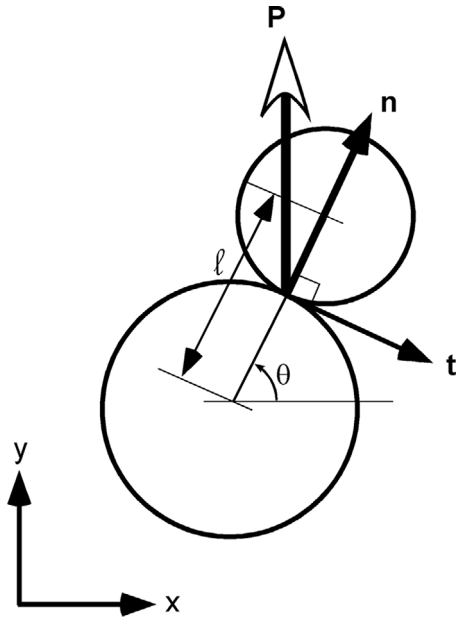

FIGURE 3 Contact normal **n**, tangential direction **t**, and contact force **P**

model accounted for inherent anisotropy[25] is one of the most promising examples for describing such behavior. This is because the model idealizes the behavior of granular materials based on a multitude of virtual simple shear mechanisms, each of which is oriented in an arbitrary direction,[21–24] and can express the tendency for larger strain components to appear in the soft and weak direction than in the hard and strong direction. Also, the mechanism has the potential to describe the noncoaxial behavior of soil with induced fabric anisotropy under monotonic/cyclic and complicated loading paths (eg, the rotation of the principal stress axis).[34,35] It is also noted that the model can be regarded as a natural extension of the existing model for orthotropic linear elastic materials to the nonlinear domain, as explained in Appendix A.

The present study aims to demonstrate the capability of a strain space multiple mechanism model with a focus on its ability to characterize the noncoaxial behavior of inherently anisotropic granular materials. As mentioned above, the model has been expanded by incorporating a new function with additional parameters to represent the effect of inherent anisotropy; its fundamental capability to evaluate the granular material behavior under monotonic proportional loading has been demonstrated.[25] However, the behavior of inherently anisotropic materials under more complex-loading conditions (eg, nonproportional loading including the rotation of the principal stress axis) was not studied in the article; rather, it was left for future work. Hence, the present study investigates the model's capability by comparing laboratory tests under various loading conditions (ie, monotonic proportional and nonproportional loadings including the rotation of the principal stress axis) with its simulations considering inherent anisotropy. Furthermore, the influence of inherent anisotropy (ie, the anisotropic parameters) on soil behavior under such loading conditions is numerically investigated. It is noted that an unloading process, particularly in the plastic region, is an essential feature to understand the cyclic behavior of anisotropic granular materials with unloading-reloading cycles[20]; however, this article focuses on the anisotropic responses during loading processes (including the rotation of the principal stress axis), with the study on the unloading process being left for future work.

2 | STRAIN SPACE MULTIPLE MECHANISM MODEL ACCOUNTING FOR INHERENT ANISOTROPY

For simplicity, the discussion in this article is limited to two dimensions, with a three-dimensional study being left for future work. The macroscopic effective stress in granular materials defined for a continuum is represented by a certain average of the contact forces between particles. As shown in Figure 3, the contact force between plane circular particles, **P**, can be partitioned into the contact normal direction, **n**, and the tangential direction, **t**, using the following equation:

$$\mathbf{P} = f_n \mathbf{n} + f_t \mathbf{t}, \tag{1}$$

where the direction vectors are given using the angle, θ, measured relative to the x-axis:

$$\mathbf{n}^T = \left[\cos\theta \ \sin\theta\right], \quad \mathbf{t}^T = \left[\sin\theta \ -\cos\theta\right]. \tag{2}$$

Macroscopic effective stress is expressed by taking the average of the contact forces within a representative volume element.[36,37] Following Rothenburg and Bathurst,[38] this average can be given in terms of the contact density (ie, the total number of assembly contacts per unit volume) m_v, the average branch length $\bar{l}_0$, and the contact-distribution function $E(\theta)$:

$$\boldsymbol{\sigma}' = m_v \bar{l}_0 \left[\int_0^{2\pi} F^*(\theta-\theta_0) f_n(\theta) E(\theta) \mathbf{n}\otimes\mathbf{n} \mathrm{d}\theta + \int_0^{2\pi} F^*(\theta-\theta_0) f_t(\theta) E(\theta) \mathbf{t}\otimes\mathbf{n} \mathrm{d}\theta\right], \tag{3}$$

where

$$\int_0^{2\pi} E(\theta)\,\mathrm{d}\theta = 1, \tag{4}$$

$$F^*(\theta) = 1 + a_1\cos 2\theta + a_2\cos 4\theta. \tag{5}$$

The symbols for expressing the contact forces' components, f_n and f_t, in Equation (1) are redefined in Equation (3) in terms of the average of the contacts in the direction θ. The function $F^*(\theta)$ has been newly introduced to account for the effect of inherent anisotropy using three additional parameters; a_1 and a_2 control the degree of inherent anisotropy, whereas θ_0 expresses the principal direction of inherent anisotropy.[25] To express the fabric of air-pluviated samples in geotechnical laboratory tests, θ_0 should be set to 90° as the normal vector direction of the bedding plane relative to the x-axis. When the anisotropic parameters are ignored, the second-order fabric tensor in Equation (3) is reduced to the formulation for inherently isotropic materials.[24]

The equilibrium of momentum is as follows:

$$\int_0^{2\pi} f_t(\theta) E(\theta) (\mathbf{t}\otimes\mathbf{n} - \mathbf{n}\otimes\mathbf{t})\,\mathrm{d}\theta = 0. \tag{6}$$

Considering this, Equation (3) can be simplified as a combination of the isotropic and deviator components with $\omega = 2\theta$ as follows:

$$\boldsymbol{\sigma}' = -p'\mathbf{I} + \frac{1}{2}\int_0^{2\pi} q \langle \mathbf{t}\otimes\mathbf{n}\rangle \,\mathrm{d}\omega, \tag{7}$$

where

$$\langle \mathbf{t}\otimes\mathbf{n}\rangle = \begin{bmatrix} \cos\omega & \sin\omega \\ \sin\omega & -\cos\omega \end{bmatrix}, \tag{8}$$

$$p' = -\frac{1}{2} m_v \bar{l}_0 \bar{f}_0, \tag{9}$$

$$\bar{f}_0 = \int_0^{2\pi} f_n(\theta) E(\theta)\,\mathrm{d}\theta, \tag{10}$$

$$q = F^* \left(\frac{\omega}{2} - \frac{\omega_0}{2} \right) q_{Iso}(\omega) + q_{Aniso}(\omega), \tag{11}$$

$$q_{Iso}(\omega) = m_v \bar{l}_0 \left[\left\{ f_n \left(\frac{\omega}{2} \right) E \left(\frac{\omega}{2} \right) - \bar{f}_0 \bar{E}_0 \right\} + f_t \left(\frac{\omega}{2} + \frac{\pi}{4} \right) E \left(\frac{\omega}{2} + \frac{\pi}{4} \right) \right], \tag{12}$$

$$q_{Aniso}(\omega) = \frac{1}{2\pi} \left\{ F^* \left(\frac{\omega}{2} - \frac{\omega_0}{2} \right) - 1 \right\} m_v \bar{l}_0 \bar{f}_0 = -\frac{1}{\pi} \{ a_1 \cos(\omega - \omega_0) + a_2 \cos 2(\omega - \omega_0) \} p', \tag{13}$$

and the average contact distribution, $\bar{E}_0$, is given by

$$\bar{E}_0 = \frac{1}{2\pi}. \tag{14}$$

As shown in Equation (11), in a multitude of virtual simple shear mechanisms oriented in an arbitrary direction, the virtual simple shear stress q depends on the normal and tangential components of interparticle contact forces f_n and f_t as well as the contact distribution function $E(\theta)$; the contact forces evolve independently during various loading processes as studied under inherently isotropic conditions by Iai et al.[34] By introducing the anisotropic function $F^*(\theta)$ in the expression, the evolution of induced fabric in inherently anisotropic granular materials changes from the fabric evolution in isotropic granular materials without inherent anisotropy, depending on the newly introduced parameters a_1, a_2, and θ_0. For a better understanding of the performance of the strain space multiple mechanism model accounting for inherent anisotropy, the anisotropic parameters' influence on macroscopic stress/strain responses is discussed in this article; however, the evolution of induced fabric, due to changes in the macroscopic stress and strain during a loading process, should be further examined by future work, for example, through comparison with discrete element simulations.

In the integrated form (ie, the direct stress-strain relationship) of the strain space multiple mechanism model (Equation 7), the macroscopic strain tensor, $\boldsymbol{\varepsilon}$, is related to the macroscopic effective stress tensor, $\boldsymbol{\sigma}'$, as follows: First, the volumetric strain, ε (extension positive), and the virtual simple shear strain, γ, are defined as a projection of the macroscopic strain to second-order tensors $\mathbf{I}$ and $\langle \mathbf{t} \otimes \mathbf{n} \rangle$, respectively, as given below:

$$\varepsilon = \mathbf{I} : \boldsymbol{\varepsilon}, \tag{15}$$

$$\gamma = \langle \mathbf{t} \otimes \mathbf{n} \rangle : \boldsymbol{\varepsilon}. \tag{16}$$

In addition, the effective volumetric strain, ε', is introduced as

$$\varepsilon' = \varepsilon - \varepsilon_d, \tag{17}$$

to account for the effect of volumetric strain due to dilatancy, ε_d, which is decomposed into contractive and dilative components. The dilative component of dilatancy is expressed as the volumetric strain component of the energy-less strain (ie, the strain that occurs due to nontouching particles)[39] based on the relationship between microscopic and macroscopic strain energies within the framework of the strain space multiple mechanism model. As explained by Ueda and Iai,[25] the dilative component is influenced by the additional anisotropic parameters; however, the contractive component of dilatancy is assumed not to be directly affected by inherent anisotropy. The contractive component is given based on the hypothesis that the micromechanical counterparts are associated with the virtual simple shear strain.[24]

The scalar variables in Equations (17) and (16) are used to define the isotropic stress, p', in Equation (9) and the isotropic component of the virtual simple shear stress, q_{Iso}, in Equation (12) as follows:

$$p' = p'(\varepsilon'), \tag{18}$$

$$q_{Iso} = q_{Iso}\left(\gamma\left(\omega\right)\right). \tag{19}$$

The virtual simple shear mechanism in the strain space multiple mechanism model is formulated as a nonlinear hysteretic function, where the backbone curve is expressed by a hyperbolic function[40]:

$$q_{Iso}\left(\gamma\left(\omega\right)\right) = \frac{\gamma\left(\omega\right)/\gamma_v}{1+\left|\gamma\left(\omega\right)/\gamma_v\right|} q_v, \tag{20}$$

where the parameters q_v and γ_v are the shear strength and the reference strain of the virtual simple shear mechanism, respectively.[22,24] These shear strength and reference strain of virtual simple shear mechanism are identified as functions of the parameters representing inherent anisotropy.[25] Therefore, out of the three transformation steps: (a) $\gamma \mapsto \gamma/\gamma_v$, (b) $\gamma/\gamma_v \mapsto q_{Iso}/q_v$, and (c) $q_{Iso}/q_v \mapsto q_{Iso}$ in Equation (20), steps (a) and (c) are influenced by inherent anisotropy. However, such anisotropy does not affect step (b), which represents the nonlinear evolution of stress-space fabric (ie, stress-induced anisotropy).[34,35] Thus, the inherent anisotropy and the stress-induced anisotropy are systematically incorporated in the strain space multiple mechanism model in the simple transformation in Equation (20).

Equations (16) and (20) with Equation (8) yield the following equalities governing the virtual simple shear strain and stress:

$$\gamma\left(\omega+\pi\right) = -\gamma\left(\omega\right), \tag{21}$$

$$q_{Iso}\left(\omega+\pi\right)/q_v = -q_{Iso}\left(\omega\right)/q_v. \tag{22}$$

By considering the above antisymmetric nature, Equation (7) can be finally rewritten as follows:

$$\boldsymbol{\sigma}' = -p'\mathbf{I} + \int_0^{\pi} q\left\langle \mathbf{t}\otimes\mathbf{n}\right\rangle \mathrm{d}\omega, \tag{23}$$

where

$$q = F\left(\omega-\omega_0\right) q_{Iso}\left(\omega\right) + q_{Aniso}\left(\omega\right), \tag{24}$$

$$F\left(\omega\right) = 1 + a_2\cos 2\omega, \tag{25}$$

$$q_{Aniso}\left(\omega\right) = -\frac{1}{\pi} a_1 \cos\left(\omega-\omega_0\right) p'. \tag{26}$$

The original anisotropic function, F^*, in Equation (5) is replaced by the different function, F, in Equation (25). As shown in Equations (25) and (26), the anisotropic parameter a_2 only affects the function F, which acts on the isotropic fabric term q_{Iso} as an anisotropic scaling factor to account for the effect of inherent anisotropy. However, the parameter a_1 only influences the additional anisotropic term q_{Aniso}.

As discussed in Ueda and Iai,[25] the macroscopic elastic shear modulus, G_m^{Aniso}, and the macroscopic shear strength, τ_m^{Aniso}, with the effect of inherent anisotropy under strain-controlled multidirectional shear loading (see Figure 4A) can be analytically derived when the tensile strains are positive as follows:

$$G_m^{Aniso} = G_m^{Iso}\left\{1+\frac{1}{2}a_2\cos 2\left(\omega_0+2\alpha_\varepsilon\right)\right\}, \tag{27}$$

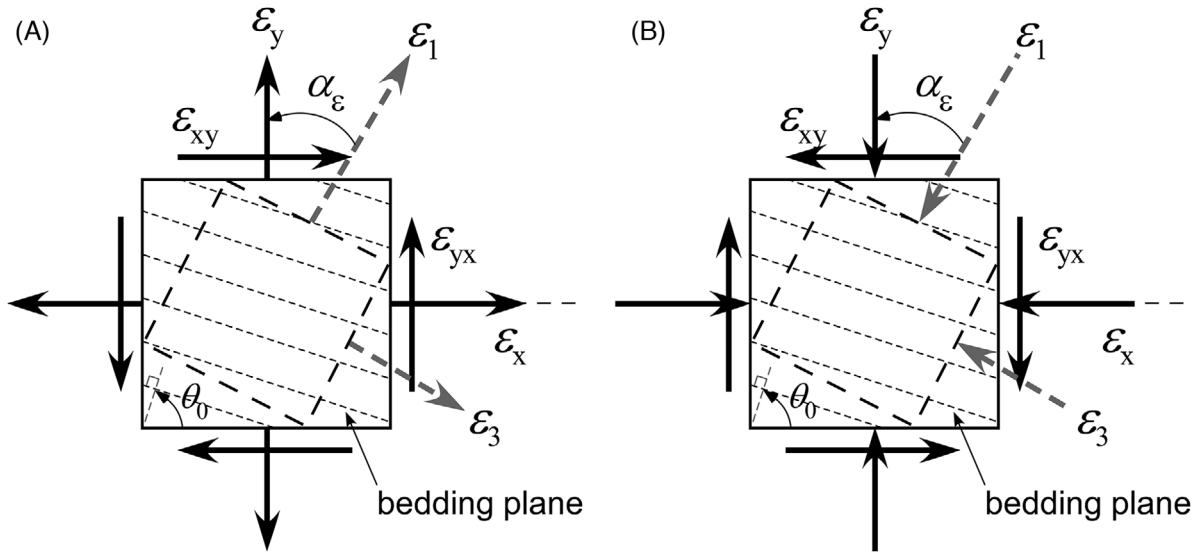

FIGURE 4 Schematic image of numerical simulation for strain-controlled multidirectional shear loading under a plane strain condition: (A) extension positive; (B) compression positive

$$\tau_m^{Aniso} = \left\{1 + \frac{1}{3}a_2 \cos 2(\omega_0 + 2\alpha_\varepsilon)\right\}\tau_m^{Iso} + \frac{1}{2}a_1 p' \cos(\omega_0 + 2\alpha_\varepsilon), \tag{28}$$

where α_ε is the major principal strain direction relative to the vertical, and the macroscopic elastic shear modulus and the macroscopic shear strength for inherently isotropic materials are given as follows[22,24]:

$$G_m^{Iso} = \frac{q_v}{\gamma_v}\int_0^\pi \sin^2\omega d\omega = \frac{\pi}{2}\frac{q_v}{\gamma_v}, \tag{29}$$

$$\tau_m^{Iso} = q_v \int_0^\pi \sin\omega d\omega = 2q_v. \tag{30}$$

When the compression strains are defined positive as shown in Figure 4B and stresses are accordingly defined as compression positive, the negative sign preceding the isotropic stress, p', is replaced with a positive sign in Equations (23) and (26) and the anisotropic macroscopic shear strength defined in Equation (28) is rewritten as

$$\tau_m^{Aniso} = \left\{1 + \frac{1}{3}a_2 \cos 2(\omega_0 + 2\alpha_\varepsilon)\right\}\tau_m^{Iso} - \frac{1}{2}a_1 p' \cos(\omega_0 + 2\alpha_\varepsilon). \tag{31}$$

The model parameters required for the complete description of the strain space multiple mechanism model accounting for inherent anisotropy are listed in Table 1. As suggested by Equation (27), the anisotropy parameter a_2 can be determined from laboratory tests for a constant deposition angle of the bedding planes, generally $\theta_0 = \omega_0/2 = 90°$ in a hollow-cylinder apparatus based on the anisotropic elastic-shear modulus G_m^{Aniso} obtained experimentally for two different principal strain directions, α_ε. Once a_2 is established, another parameter, a_1, can be determined from Equation (28) based on the shear strength corresponding to the two different principal strain directions. The remaining 15 parameters are common to the strain space multiple mechanism model without inherent anisotropy[24]; these parameters, in particular the dilatancy parameters, can be calibrated by referring to laboratory test results (eg, stress-strain relationship, stress path) under undrained monotonic and/or cyclic loading.

TABLE 1 Model parameters of the strain space multiple mechanism model

Symbol	Mechanism	Parameter designation
$K_{L/Ua}$	Volumetric	Bulk modulus under the confining pressure p_a
r_K	Volumetric	Reduction factor of bulk modulus for liquefaction analysis (= 0.5 in this study)
l_K	Volumetric	Power index of bulk modulus for liquefaction analysis (= 2.0 in this study)
G_{ma}^{Iso}	Shear	Isotropic shear modulus under the confining pressure p_a
ϕ_f^{Iso}	Shear	Isotropic internal friction angle
$h_{\max}$	Shear	Upper bound for hysteretic damping factor (= 0.24 in this study)
ϕ_p	Dilatancy	Phase transformation angle (= 28° in this study)
r_{ε_d}	Dilatancy	Parameter controlling dilative and contractive components
$r_{\varepsilon_d^c}$	Dilatancy	Parameter controlling contractive component
q_1	Dilatancy	Parameter controlling initial phase of contractive component
q_2	Dilatancy	Parameter controlling final phase of contractive component
ε_d^{cm}	Dilatancy	Limit of contractive component
S_1	Dilatancy	Small positive number to avoid zero confining pressure (= 0.005 in this study)
c_1	Dilatancy	Parameter controlling elastic range for contractive component
q_{us}	Dilatancy	Undrained shear strength for steady-state analysis (= ∞ in this study)
a_1	Fabric anisotropy	Parameter controlling the degree of anisotropy
a_2	Fabric anisotropy	Parameter controlling the degree of anisotropy
θ_0	Fabric anisotropy	Parameter controlling the direction of anisotropy

TABLE 2 Model parameters used for dry-pluviated Toyoura sand with a relative density of: (A) 90%, (B) 60%, and (C) 30%[9]

(A)											
$K_{L/Ua}$ (kPa)	G_{ma} (kPa)	ϕ_f (°)	r_{ε_d}	$r_{\varepsilon_d^c}$	q_1	q_2	ε_d^{cm}	c_1	a_1	a_2	θ_0 (°)
254,800	97,705	45.0	0.2	2.0	2.5	1.20	0.10	1.0	0.08	0.18	90
(p_a = 98kPa)											
(B)											
$K_{L/Ua}$ (kPa)	G_{ma} (kPa)	ϕ_f (°)	r_{ε_d}	$r_{\varepsilon_d^c}$	q_1	q_2	ε_d^{cm}	c_1	a_1	a_2	θ_0 (°)
204,704	78,495	42.0	0.2	3.0	2.5	0.75	0.15	1.0	0.08	0.18	90
(p_a = 98kPa)											
(C)											
$K_{L/Ua}$ (kPa)	G_{ma} (kPa)	ϕ_f (°)	r_{ε_d}	$r_{\varepsilon_d^c}$	q_1	q_2	ε_d^{cm}	c_1	a_1	a_2	θ_0 (°)
163,049	62,522	40.0	0.2	3.5	3.5	0.35	0.20	1.0	0.15	0.05	90
(p_a = 98kPa)											

3 | MONOTONIC PROPORTIONAL LOADING

3.1 | Simulation of undrained behavior under strain-controlled multidirection shear

The noncoaxiality between the principal directions of the stress and strain tensors under monotonic proportional loading was briefly overviewed within the framework of the strain space multiple mechanism model by simulating undrained strain-controlled laboratory tests conducted by Nakata et al[9] for dry-pluviated Toyoura sand (see appendix B in Ueda and Iai[25]). In the present study, simulations without inherent anisotropy were performed in addition to those with inherent anisotropy using the model parameters in Table 2 to shed light on the influence of inherent anisotropy on noncoaxial behavior. The (isotropic) small-strain shear modulus, G_m^{Iso}, under an arbitrary confining pressure, p, was estimated through an empirical relation[41] as follows:

$$G_m^{Iso} = G_{ma}\left(\frac{p}{p_a}\right)^{0.5}, \quad G_{ma} = 7000\frac{(2.17-e)^2}{1+e}p_a^{0.5}, \tag{32}$$

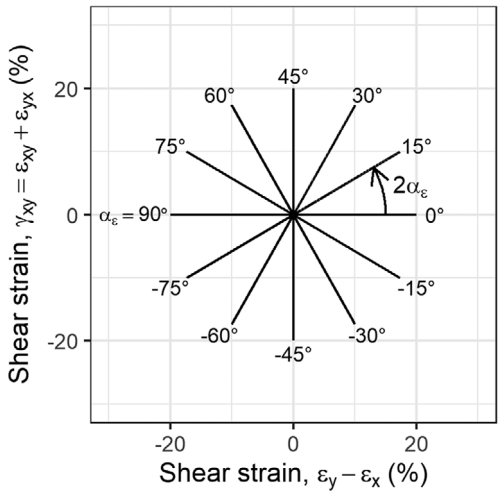

FIGURE 5 Deviator strain path applied in simulations of undrained monotonic behavior under multidirectional shear loading

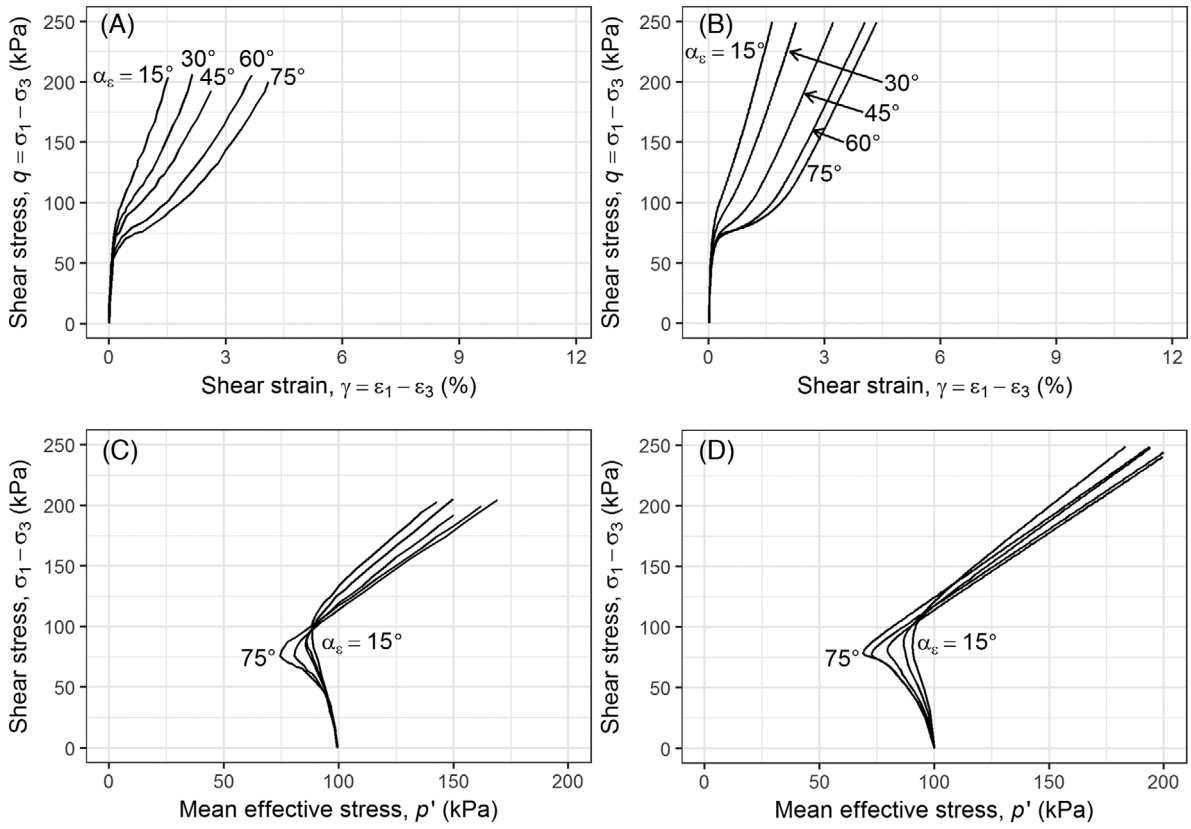

FIGURE 6 Experimental results[9] and model simulations[23] for undrained torsional shear tests of Toyoura sand with a relative density of 90%: (A) measured stress-strain relationship; (B) computed stress-strain relationship; (C) measured stress path; (D) computed stress path

where G_{ma} is the small-strain shear modulus under the reference confining pressure, p_a (= 98 kPa in this case).

Monotonic strain loadings were applied at different angles relative to the horizontal bedding plane as shown in Figure 5. The measured stress-strain relationship and effective stress path for a relative density of 90%, 60%, and 30% are presented in Figures 6-8, respectively, with those simulated considering inherent anisotropy. The model is capable of capturing the essential features of laboratory test data under monotonic proportional loading by introducing the anisotropic parameters: the experimental trend that inherent anisotropy with a larger α_ε value results in softer (ie, smaller shear stress at the same

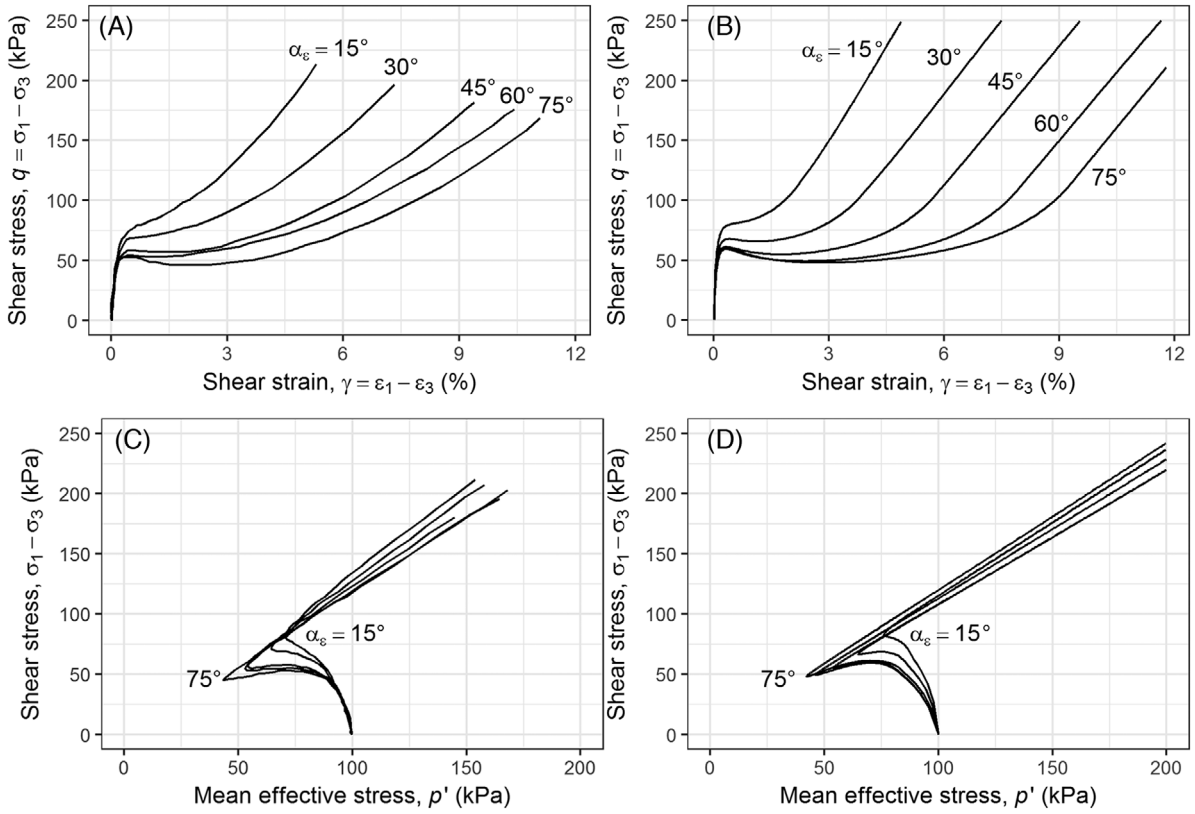

FIGURE 7 Experimental results[9] and model simulations[23] for undrained torsional shear tests of Toyoura sand with a relative density of 60%: (A) measured stress-strain relationship; (B) computed stress-strain relationship; (C) measured stress path; (D) computed stress path

shear strain) and more contractive responses is properly simulated. Shear failure envelop is accordingly affected by the inherent anisotropy.

To analyze in more detail the deviator stresses presented in terms of principal stress direction's difference in Figures 6–8, the deviator stresses are decomposed into stress components of $(\sigma'_y - \sigma'_x)/2$ and τ_{xy} as shown in Figure 9. In this figure, the stress components are normalized with p' to study the direction of stress components in this deviator plane throughout the undrained test; solid lines indicate the response with inherent anisotropy, while dotted lines indicate the response without inherent anisotropy. In the figure, the anisotropic Mohr's circle, which was calculated by normalizing Equation (31) with the isotropic stress p', is also shown; compared with the isotropic Mohr's circle, the anisotropic Mohr's circle is distorted in shape due to the anisotropic model parameters a_1 and a_2. Comparison of the isotropic stress path with the corresponding applied strain path in Figure 5 reveals that the principal stress direction, α_σ, which can be calculated from the stress paths and is the same as the principal stress increment direction, $\alpha_{d\sigma}$, under proportional loading, is found to be identical (or coaxial) with the principal strain direction, α_ε, regardless of the relative density as shown in Figure 10. However, by employing the anisotropy parameters, α_σ becomes different from α_ε except when $\alpha_\varepsilon = 0°$ and 90°. These simulations demonstrate that the noncoaxiality between α_σ (or $\alpha_{d\sigma}$) and α_ε under monotonic proportional shear loading becomes prominent when the effect of inherent anisotropy is considered. It was also found that soil response becomes completely coaxial irrespective of whether inherent anisotropy exists, when α_ε is coincident with or perpendicular to the direction of the bedding plane (eg, $\alpha_\varepsilon = 90°$ or 0° with $\theta_0 = 90°$ as seen in Figure 4) even though the failure strength is influenced by inherent anisotropy.

3.2 | Simulation of drained behavior under stress-controlled multidirectional shear

Regarding the noncoaxiality between α_σ (or $\alpha_{d\sigma}$) and α_ε under proportional multidirectional loading, laboratory tests similar to those conducted by Nakata et al[9] were also performed by Gutierrez et al[3] but under a drained and stress-controlled condition. They reported the experimental failure points by plotting the peak shear stress in each

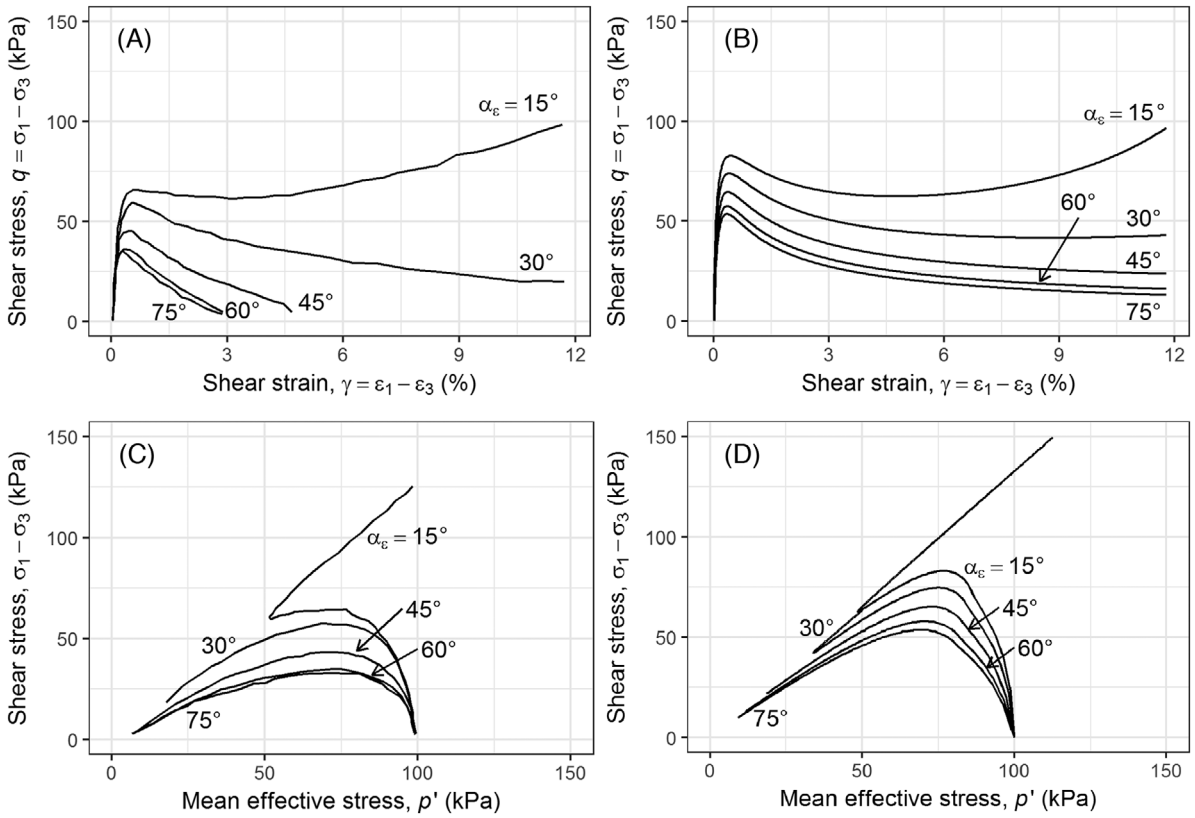

FIGURE 8 Experimental results[9] and model simulations[23] for the undrained torsional shear tests of Toyoura sand with a relative density of 30%: (A) measured stress-strain relationship; (B) computed stress-strain relationship; (C) measured stress path; (D) computed stress path

test in deviator stress space as shown in Figure 11; the effect of the loading direction on the shear strength is clearly observed. Hence, the model constants, in particular the anisotropic parameters a_1 and a_2 as well as the (isotropic) internal friction angle ϕ_f, were calibrated to represent the experimental shear strength (Table 3) accurately. Among these parameters, a_1 primarily acts to shift the location of the model failure surface whereas a_2 primarily acts to distort the model failure surface as inferred from Equation (31). As shown in Figure 11, the anisotropic Mohr's circle obtained from Equation (31) almost satisfies the experimental trend. As for the small-strain shear modulus in the table, Equation (32) was used.

Figures 12B and C illustrate simulated strain responses along with the applied stress paths A through E, with and without considering inherent anisotropy, respectively, using the parameters in Table 3. It is noted that the plastic strain increment considering inherent anisotropy, expressed by solid arrows in Figure 12B, was calculated by subtracting the anisotropic elastic strain increments, which were obtained from the applied stress increment using the anisotropic elastic shear modulus, G_m^{Aniso}, in Equation (27), from the simulated total strain increments. Meanwhile, dotted arrows in Figure 12B were calculated by subtracting the isotropic elastic strain increments, assuming the isotropic elastic shear modulus, G_m^{Iso}, although the shear modulus used in the simulation was anisotropic due to the anisotropic model parameter a_2 (see Equation 27). The purpose of this is to ensure the same condition as the experiment (Figure 12A) for model validation; Gutierrez et al[3] simply used the isotropic Young's modulus and Poisson's ratio (ie, $E = E_x = E_y = E_z$ and $\nu = \nu_{yz} = \nu_{zx} = \nu_{xy}$ in Equations 34–37) for calculating the elastic strains.

The simulated responses without inherent anisotropy in Figure 12C are found not to accurately capture the measured noncoaxiality between α_σ (or $\alpha_{d\sigma}$) and the principal direction of the plastic strain increment, $\alpha_{d\varepsilon^p}$, in the early stage of loading, particularly for paths A and E. However, the anisotropic simulation using G_m^{Iso} (dotted arrows in Figure 12B) is capable of capturing the experimental (apparent) noncoaxial response. In fact, the experimental plastic responses in Figure 12A are likely not to represent the actual behavior in the early stage of loading, where the elastic strain is dominant compared to the plastic one; this is because the elastic strain should be inherently anisotropic (or $\alpha_{d\varepsilon^e}$ is noncoaxial with $\alpha_{d\sigma}$ shown in Figure 2C). Thus, the solid arrows using G_m^{Aniso} in Figure 12B may be more representative of the actual plastic responses. As the stress path approaches the failure surface in Figure 12B, the directions of anisotropic plastic strain

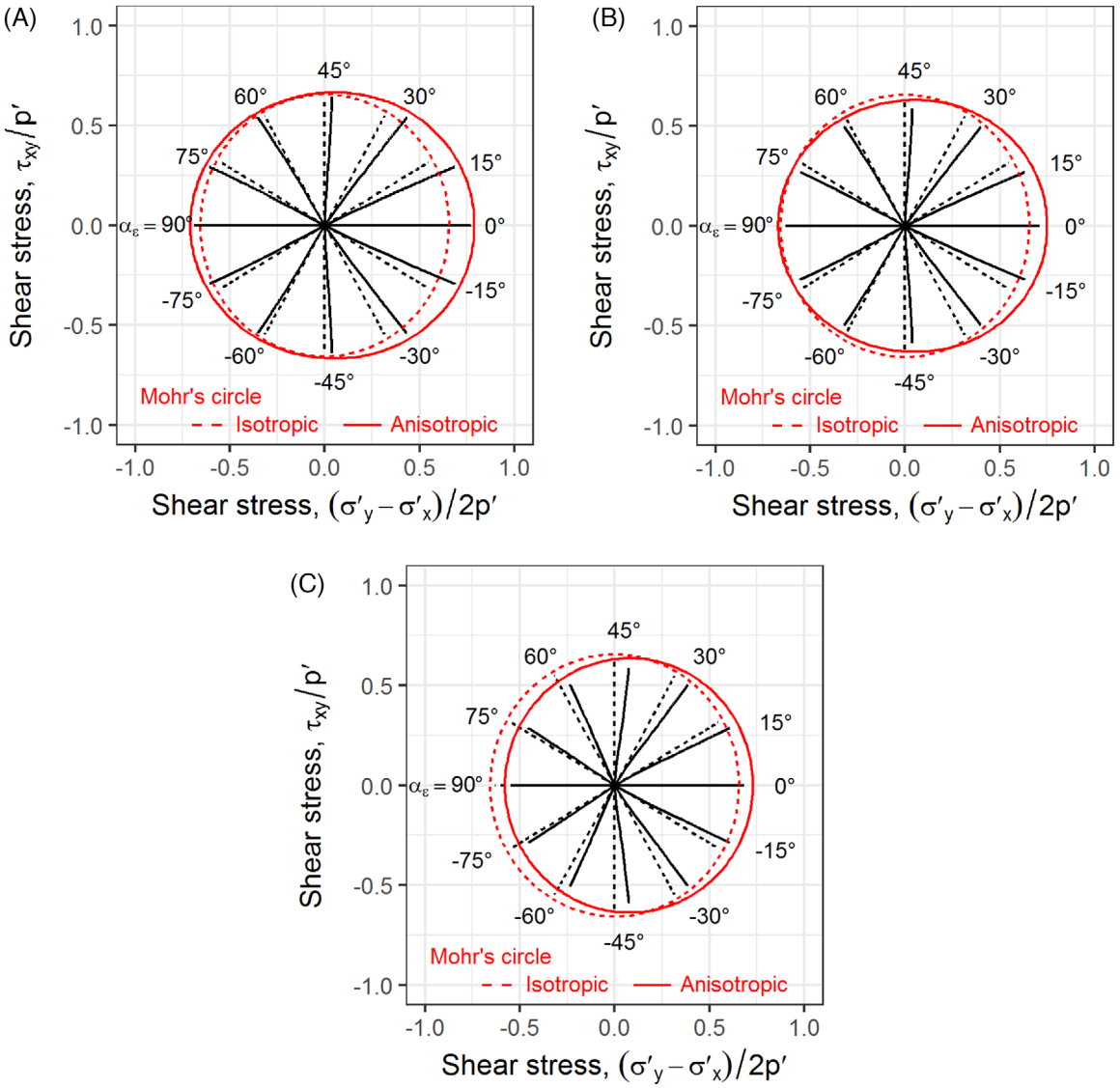

FIGURE 9 Deviator stress paths obtained from the undrained multidirectional-shear loading simulation of Toyoura sand with a relative density of: (A) 90%; (B) 60%; and (C) 30%

increments become closer to each other, regardless of how the elastic strain is calculated. Also, the simulated direction of plastic strain increment tends to approach the coaxiality with the applied principal stress (or stress increment) direction; this tendency between $\alpha_{d\varepsilon^p}$ and α_σ (or $\alpha_{d\sigma}$) was also observed in the experiment, but different from the perfect coaxiality in Figure 12C.

For better understanding, Figure 13 compares simulated $\alpha_{d\varepsilon^p}$ changes in response to the applied deviator stress ratio with the experimental plots; as described earlier, G_m^{Iso} is used for Figure 13A, instead of G_m^{Aniso}, to calculate the elastic strain increment in the same way as in the experiment. The figure demonstrates that the simulation in Figure 13A can reasonably capture the experimental change of $\alpha_{d\varepsilon^p}$ along with each stress path by introducing the anisotropic model parameters (a_1, a_2, and θ_0) in Table 3. However, both the simulated and measured $\alpha_{d\varepsilon^p}$ may not represent the actual plastic behavior because of G_m^{Iso} being used for deriving the plastic strain increment. Note that a kink appeared in the early stage of the loading paths A, B, and E in Figure 13A may be due to the inconsistency between the actual G_m^{Aniso} and the assumption of G_m^{Iso} used to calculate $\alpha_{d\varepsilon^p}$. Figure 14 illustrates the relationship of simulated $\alpha_{d\varepsilon^p}$ with the principal directions of simulated total and elastic strain increments, $\alpha_{d\varepsilon}$ and $\alpha_{d\varepsilon^e}$. Comparison of Figure 14A with Figure 14B demonstrates that $\alpha_{d\varepsilon^p}$ in the early stage of loading strongly depends on how to calculate the elastic strain (or elastic shear modulus). It is also found that the introduction of the anisotropic model parameters is essential to consider, as the stress ratio increases (ie, the stress path approaches the failure surface), for evaluating the plastic behavior of inherently anisotropic granular materials.

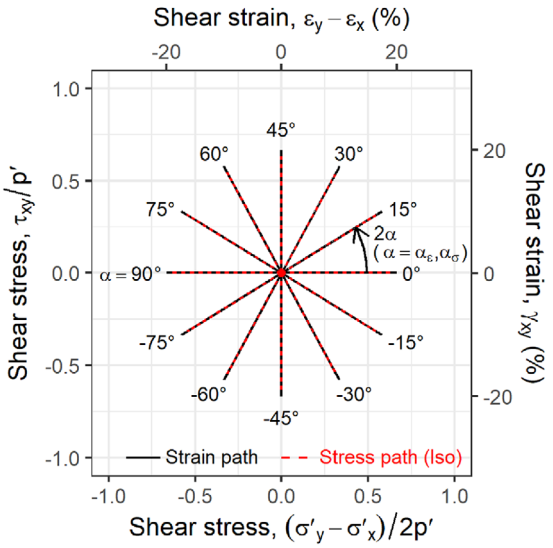

FIGURE 10 Coaxiality between applied deviator strain paths and corresponding simulated deviator stress paths without inherent anisotropy under the undrained multidirectional-shear loading of Toyoura sand with a relative density of 90%, 60%, and 30%

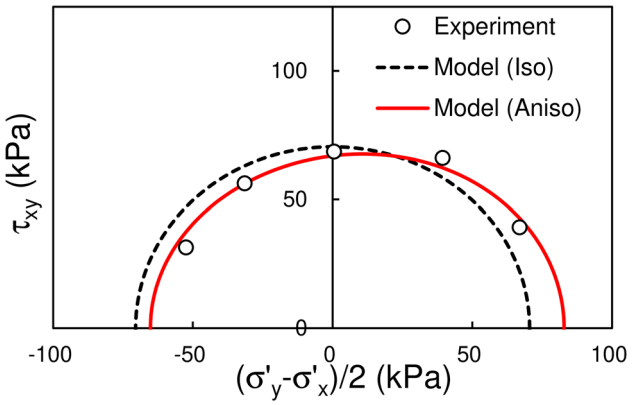

FIGURE 11 Experimental failure points[3] and model failure surface (Mohr's circle) considering inherent anisotropy

4 | MONOTONIC NONPROPORTIONAL LOADING

Monotonic loading often involves a change in both the principal stress direction and the loading magnitude. Gutierrez et al[3] also performed laboratory tests under this type of nonproportional loading, as shown in Figure 15. Along loading path A, the magnitude of stress vector monotonically increased with a change in the principal stress direction after the initial biaxial shear loading reached 50 kPa; here, the principal stress direction indicates the direction of stress vector represented by the angle $2\alpha_\sigma$. In the case of loading paths B and C, the magnitude initially decreased and then increased with a change in the principal stress direction after the initial shear. Based on the measured plastic strain increment directions in Figure 16A, $\alpha_{d\varepsilon^p}$ changes in response to the applied deviator stress ratio are illustrated as triangle plots along with α_σ (dotted lines) in Figure 17. The experimental plots demonstrate that α_σ and $\alpha_{d\varepsilon^p}$ became more noncoaxial compared with the monotonic proportional loading (see Figure 12A or the experimental plots in Figure 13) when a change in the principal stress direction was involved. In particular, the plastic strain increment along loading path C, where the

TABLE 3 Model parameters used for dry-pluviated Toyoura sand with a relative density of 70%[3]

$K_{L/Ua}$ (kPa)	G_{ma} (kPa)	ϕ_f (°)	a_1	a_2	θ_0 (°)
220,383	84,508	46.0	0.18	0.15	90

(p_a = 98kPa).

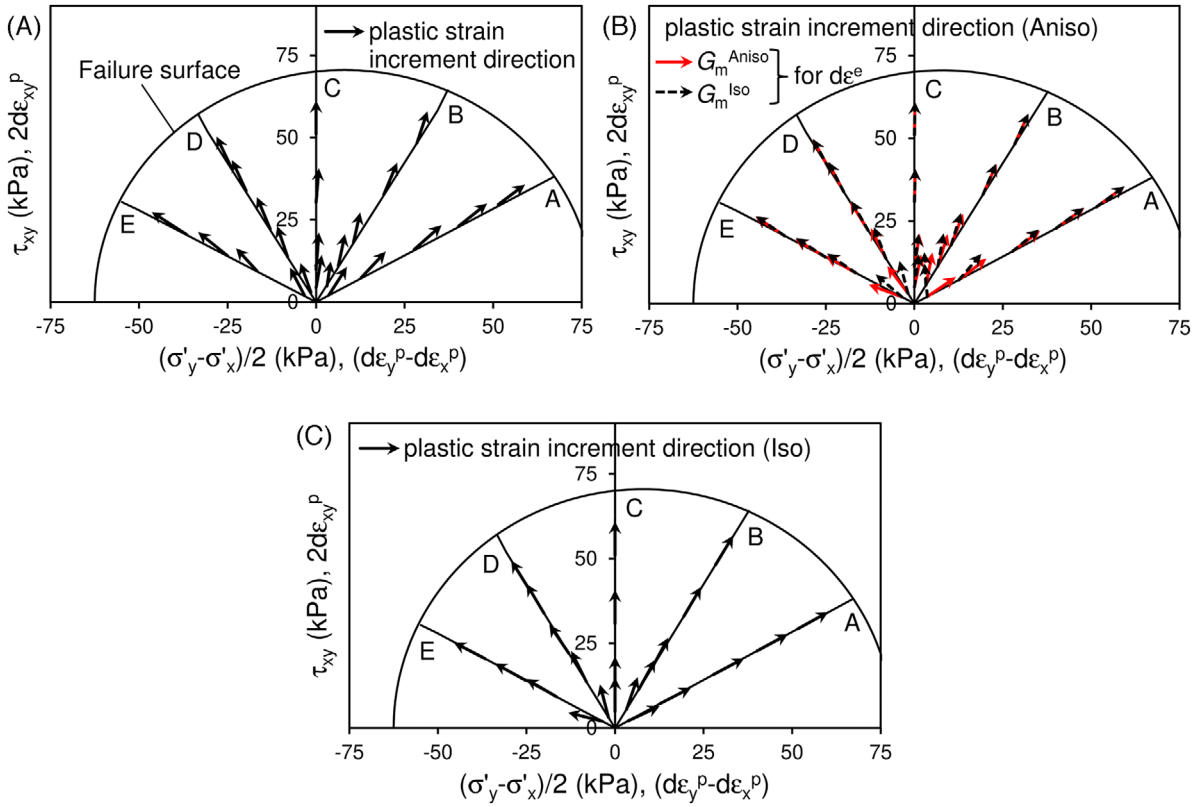

FIGURE 12 The direction of plastic strain increments during drained monotonic proportional loading: (A) experimental results[3]; (B) simulation with inherent anisotropy; (C) simulation without inherent anisotropy

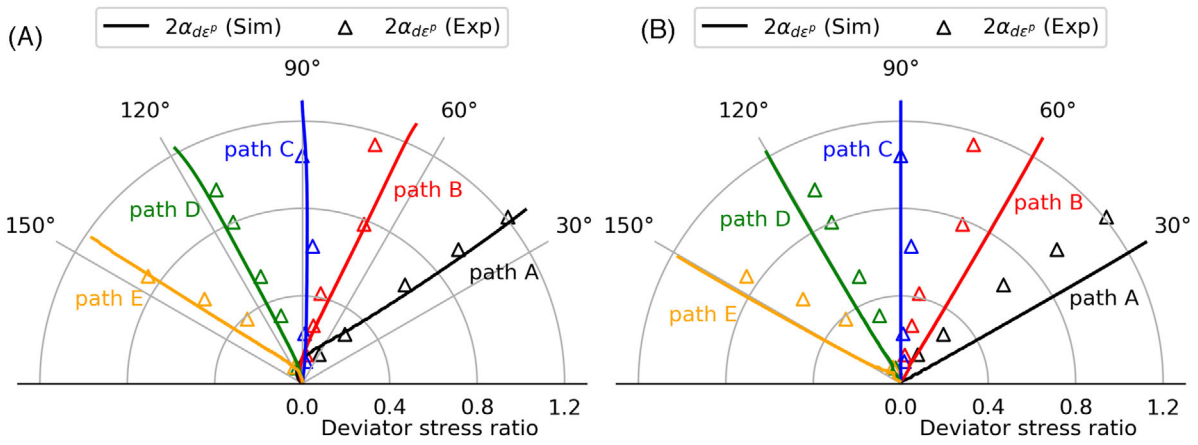

FIGURE 13 Comparison of simulated and measured principal directions of plastic strain increments against the applied deviator stress ratio during drained monotonic proportional loading: (A) with inherent anisotropy considering the isotropic elastic shear modulus; (B) without inherent anisotropy

principal stress direction rotates from 0 to $(3/4)\pi$ relative to the horizontal axis, showed the most pronounced obliquity in the principal stress direction. These loading paths were studied through simulations using the strain space multiple mechanism model with inherent anisotropy using the same model parameters given in Table 3.

Figures 16B and 16C illustrate the simulated direction of plastic strain increment with and without the consideration of inherent anisotropy, respectively; as described in Section 3.2, the plastic strain increment in Figure 16B was calculated by subtracting the anisotropic or isotropic elastic strain increment obtained using Equation (27) with or without the anisotropic parameter a_2, respectively, from the simulated total strain increment. For better understanding, Figure 17

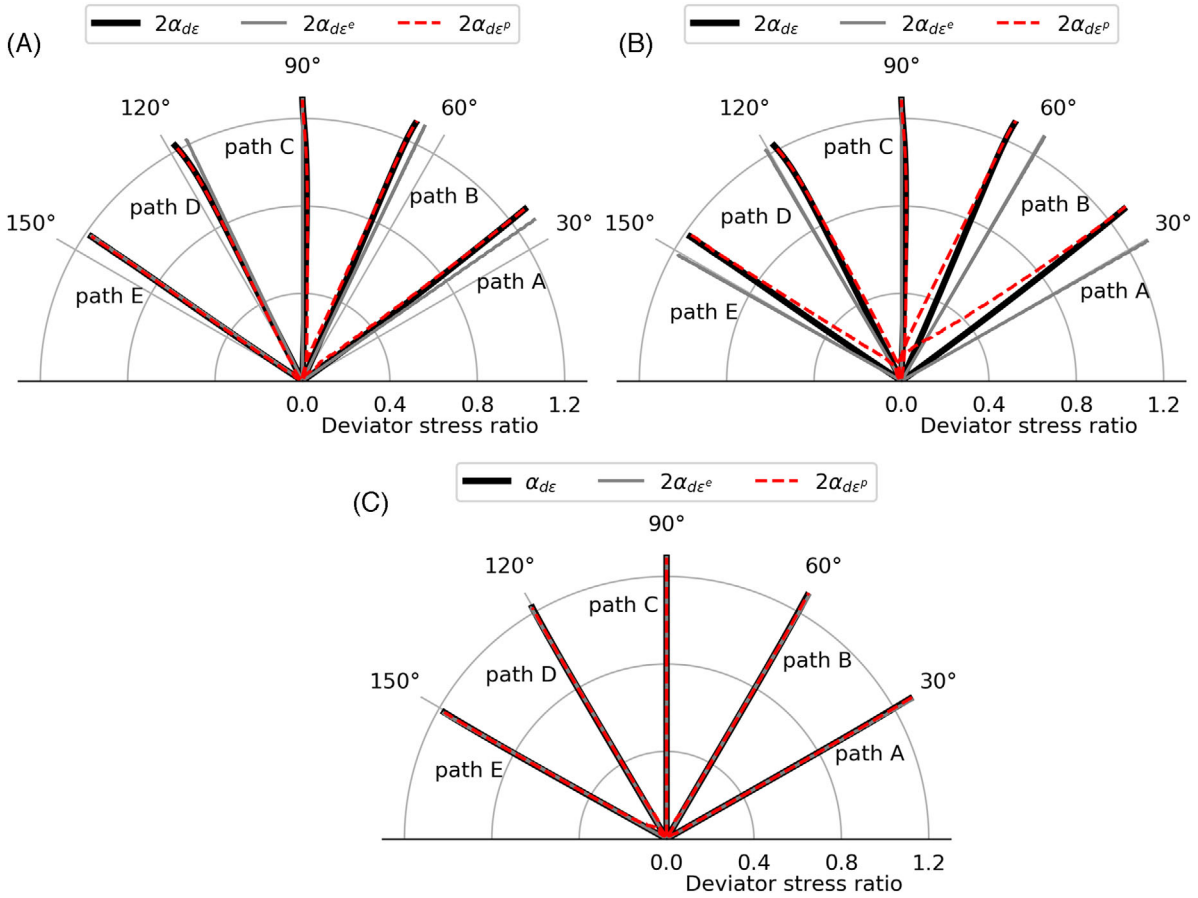

FIGURE 14 Simulated principal strain increment directions against the applied deviator stress ratio during drained monotonic proportional loading: (A) with inherent anisotropy considering the anisotropic elastic shear modulus; (B) with inherent anisotropy considering the isotropic elastic shear modulus; (C) without inherent anisotropy

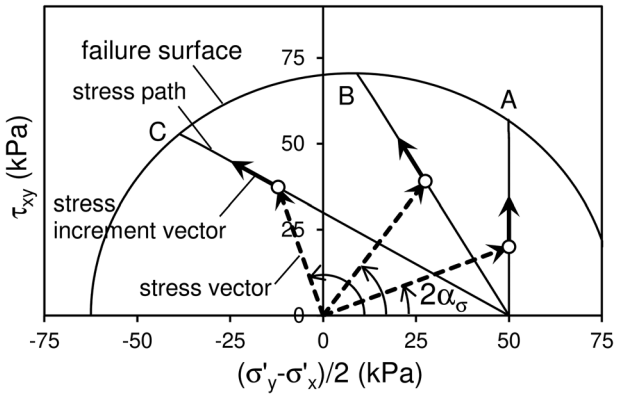

FIGURE 15 Relationship between applied straight-line stress paths[3] and the angle of principal stress direction, α_σ during monotonic nonproportional loading

compares the simulated direction, $\alpha_{d\varepsilon^p}$, with the experimental counterpart, while Figure 18 shows the relationship among the simulated $\alpha_{d\varepsilon}$, $\alpha_{d\varepsilon^e}$, and $\alpha_{d\varepsilon^p}$ along with the applied α_σ.

Along stress path A, how to calculate the elastic strain is found to exert no influence on $\alpha_{d\varepsilon^p}$ from a comparison of solid and dotted arrows in Figure 16B (or from a comparison of solid lines in Figures 18A and 18B); this is because τ_{xy} simply increases with no change in $(\sigma'_y - \sigma'_x)/2$ along the path, as is the case with the loading path C in Figure 14, and as a result $\alpha_{d\varepsilon^e}$ expressed by dotted lines in Figure 18A shows the same response as that in Figure 18B. Comparison of Figure 16B

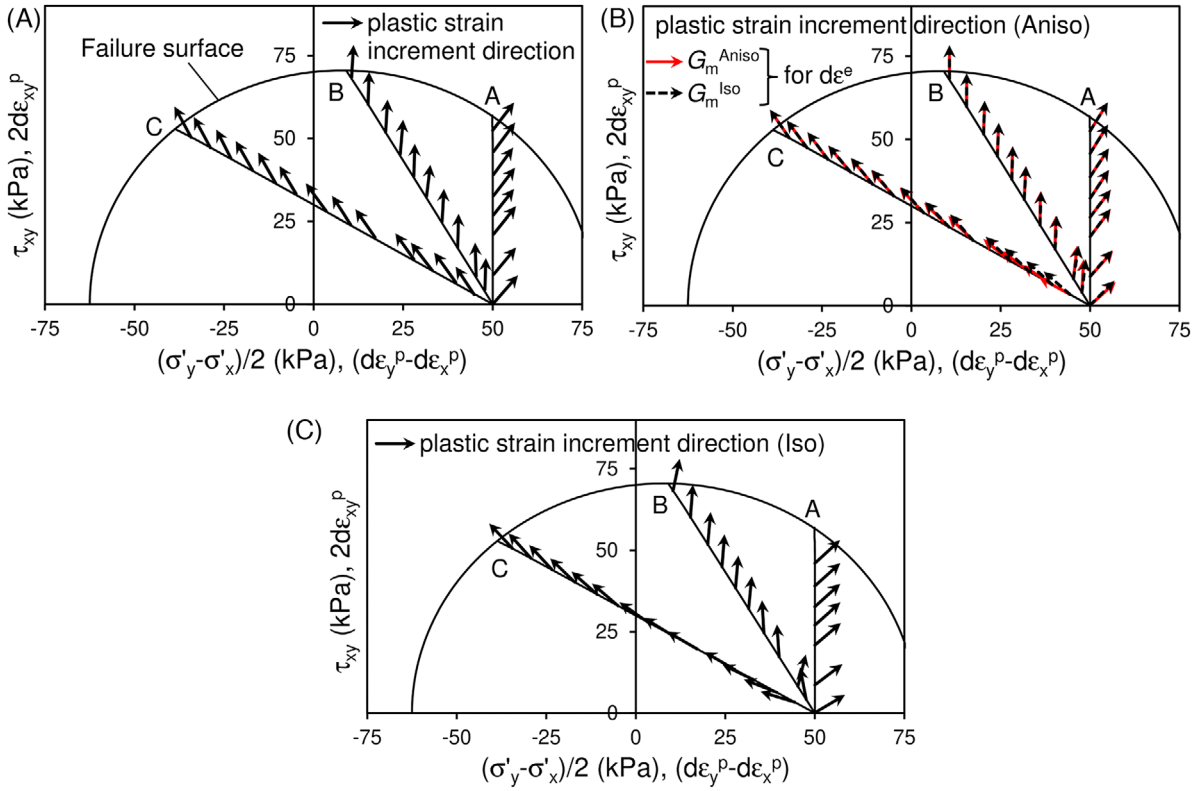

FIGURE 16 The direction of plastic strain increments during drained monotonic nonproportional loading along different straight-line stress paths: (A) experimental results[3]; (B) simulation with inherent anisotropy; (C) simulation without inherent anisotropy

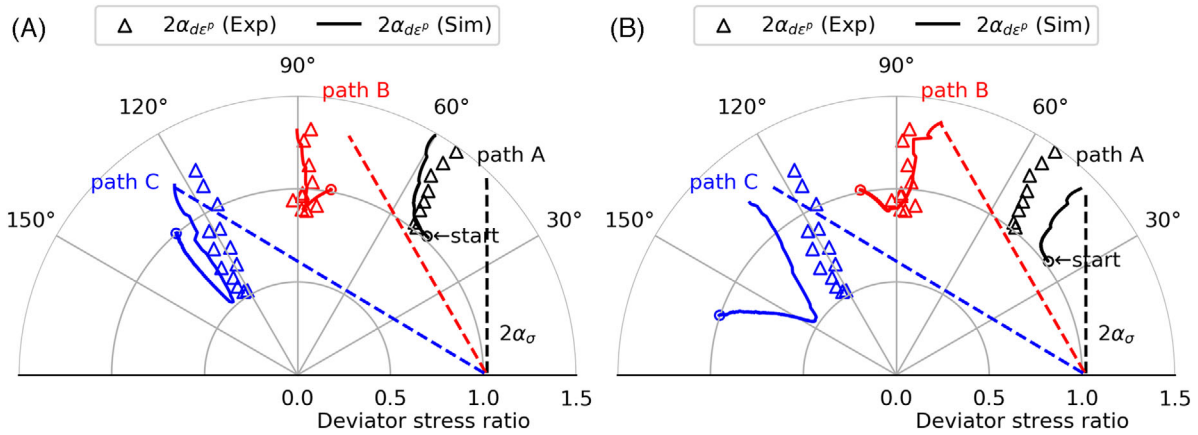

FIGURE 17 Comparison of simulated and measured principal directions of plastic strain increments during drained monotonic nonproportional loading: (A) with inherent anisotropy considering the anisotropic elastic shear modulus; (B) with inherent anisotropy considering the isotropic elastic shear modulus; (C) without inherent anisotropy

with Figure 16C demonstrates that the degree of inherent anisotropy's influence on the plastic strain increment direction seems path-independent; more specifically, the anisotropic response of $\alpha_{d\varepsilon^p}$ (Figure 17A) always has an angle about 15° (in terms of $2\alpha_{d\varepsilon^p}$) higher than the isotropic one (Figure 17B), and as a result is capable of capturing the experimental noncoaxial behavior between $\alpha_{d\varepsilon^p}$ and α_σ. The constant difference in $\alpha_{d\varepsilon^p}$ may be because the direction and magnitude of the applied stress vector do not change drastically along path A compared to paths B and C, as shown in Figure 15.

In the case of stress path B, how to calculate the elastic strain does not make a noticeable difference in $\alpha_{d\varepsilon^p}$ between Figures 18A and 18B except the early stage of nonproportional loading, although $\alpha_{d\varepsilon^e}$ in Figure 18A is always slightly less than that in Figure 18B. It is also found that the anisotropic parameters (a_1, a_2, and ω_0) exert nonnegligible effects on

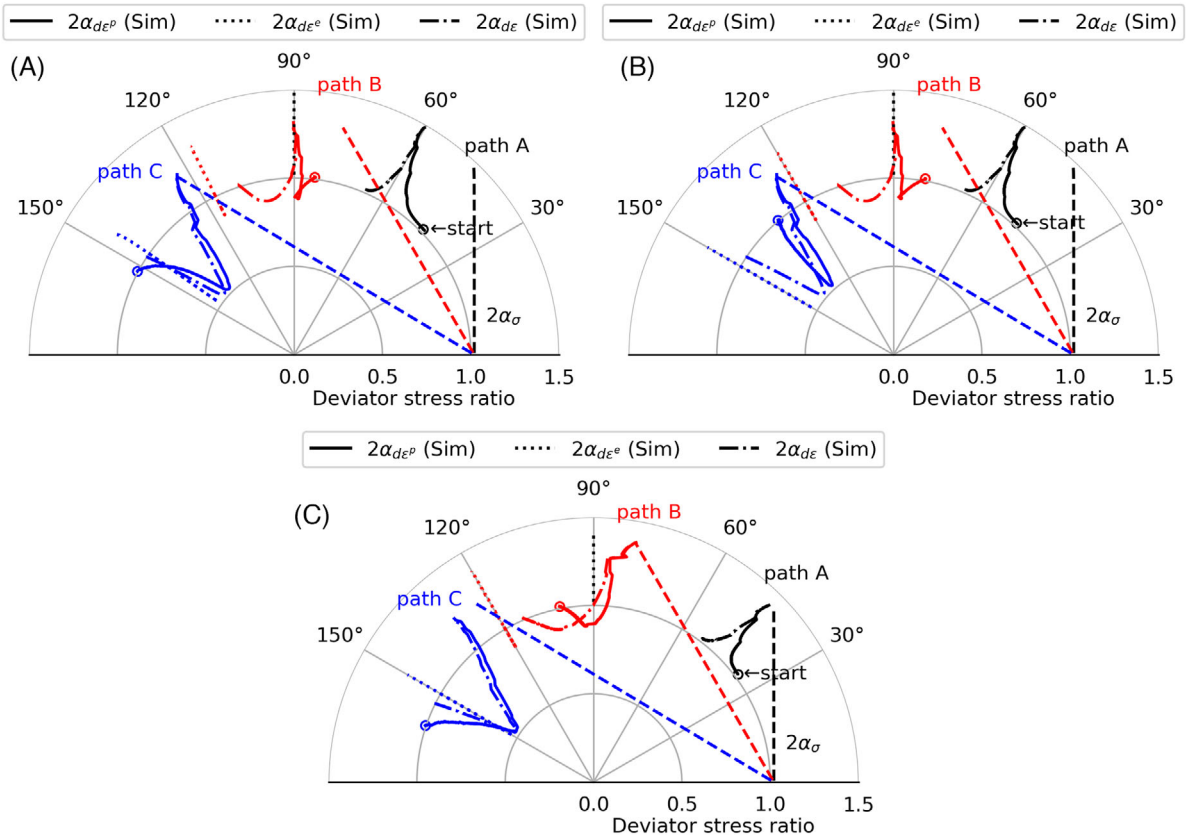

FIGURE 18 Simulated principal strain increment directions during drained monotonic nonproportional loading: (A) with inherent anisotropy considering the anisotropic elastic shear modulus; (B) with inherent anisotropy considering the isotropic elastic shear modulus; (C) without inherent anisotropy

$\alpha_{d\varepsilon^p}$ not only in the early stage but also near the failure surface, as shown in Figure 17. Consequently, the simulation considering the inherent anisotropy can adequately capture the experimental plots: the noncoaxiality between α_σ and $\alpha_{d\varepsilon^p}$, which is more prominent in the early stage of loading, gradually decreases as the stress path becomes closer to the failure surface (or the deviator stress ratio increases), but does not reach to a coaxial state.

As in the case of loading path B, the simulated $\alpha_{d\varepsilon^p}$ along stress path C with no consideration for inherent anisotropy differs from the measured $\alpha_{d\varepsilon^p}$ in Figure 17B. However, the introduction of the anisotropic model parameters (a_1, a_2, and θ_0) in Table 3 is found to reproduce the experimental $\alpha_{d\varepsilon^p}$ plots with better accuracy as shown in Figure 17A. It must be noted here that both the measured and simulated $\alpha_{d\varepsilon^p}$ in Figure 17A are likely not to represent the actual behavior of the inherently anisotropic sand; this is because the elastic strain should also be inherently anisotropic (or $\alpha_{d\varepsilon^e}$ is noncoaxial with $\alpha_{d\sigma}$) as shown in Figure 18A. Hence, the solid line in Figure 18A can be considered to represent the actual plastic behavior better than that in Figure 18B, in particular, in the process of unloading the deviator stress ratio (from the start point to the reverse one under nonproportional loading).

5 | ROTATION OF THE PRINCIPAL STRESS AXIS

After the pioneering study conducted by Arthur et al[42] on soil behavior subject to the rotation of the principal stress axis through laboratory tests, this kind of research has attracted much attention among geotechnical engineering researchers. For example, Gutierres et al[3] conducted an experimental study that focused on dry-pluviated medium-dense Toyoura sand with a relative density of 70%. In their laboratory tests, the deviator stress path illustrated in Figure 19 was applied to the soil specimen under a drained condition; the principal stress direction was rotated counterclockwise by maintaining a constant deviator stress magnitude under the initial confining stress of 98 kPa. Here, we investigated the capability of the strain space multiple mechanism model accounting for inherent anisotropy by comparing the PSR tests (Figure 20A)

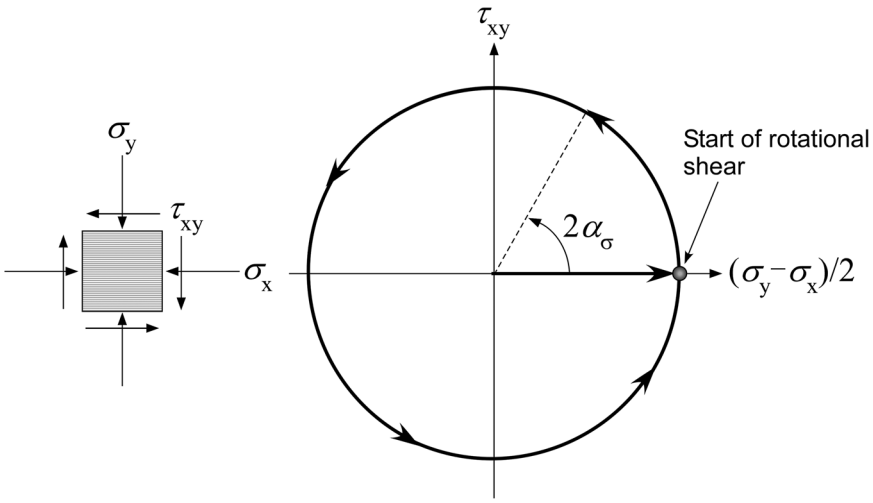

FIGURE 19 Deviator stress path for the undrained principal stress rotation tests performed by Gutierres et al[3]

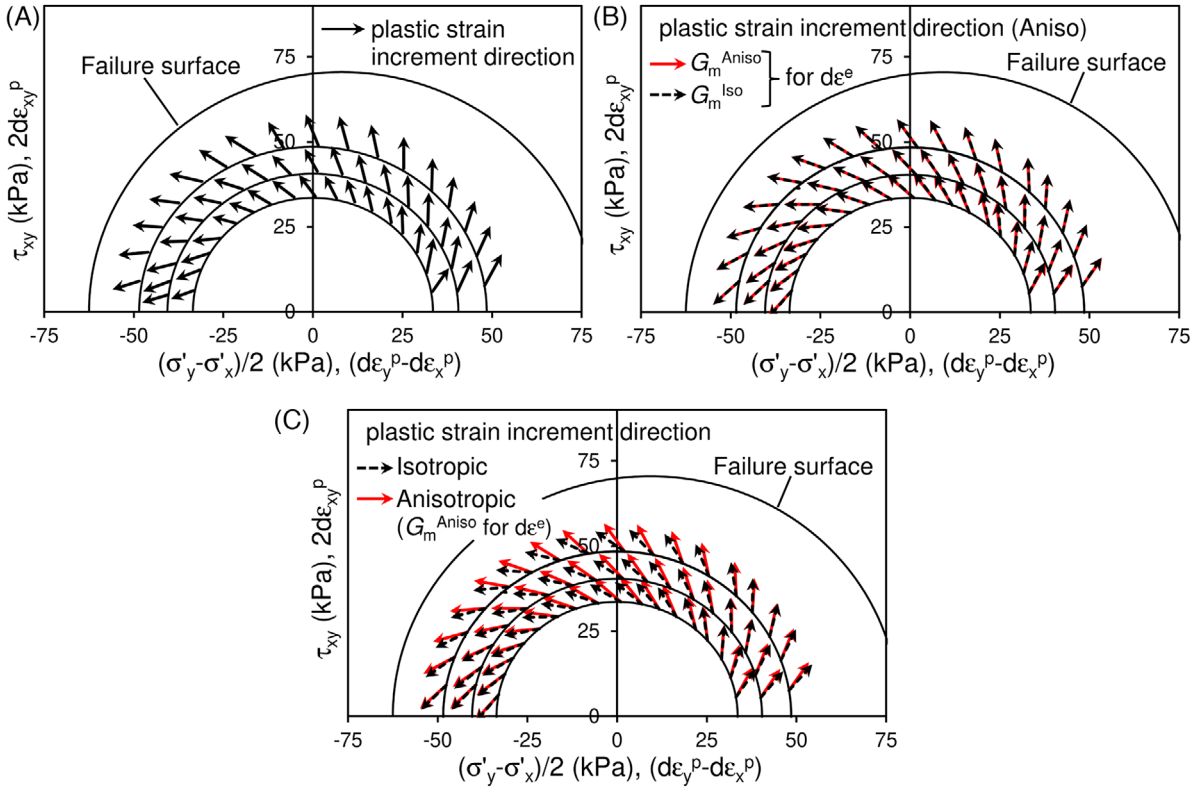

FIGURE 20 The direction of plastic strain increments during the drained principal stress rotation tests for constant mobilized friction angles of $\phi = 20°$, 25°, and 30°: (A) experimental results[3]; (B) simulation results with inherent anisotropy; (C) simulation results without inherent anisotropy

under the constant mobilized friction angles, $\phi = (\sigma_z - \sigma_\theta)/(\sigma_z + \sigma_\theta)$, between 20° and 35°. In the simulation, the model parameters given in Table 3 were used; for details regarding the setting of the parameters, refer to Section 3.2.

Figure 20B illustrates the simulated plastic strain increment direction considering inherent anisotropy, which was calculated by subtracting the anisotropic or isotropic elastic strain increment from the simulated total strain increment (refer to Section 3.2 for a reason for using the isotropic elastic strain increment), for $\phi = 20°$, 25°, and 30°. Of these simulation results, the plastic strain increment vectors for $\phi = 20°$ and 30° are redrawn with their magnitude in Figures 21A and B, including simulated total and elastic strain vectors. These figures demonstrate that how to calculate the elastic strain with or without the anisotropic parameter a_2 in Equation (27) exerts little influence on the plastic strain increment because the elastic component does not contribute as much to the total strain compared to the plastic one. Comparing the simulated

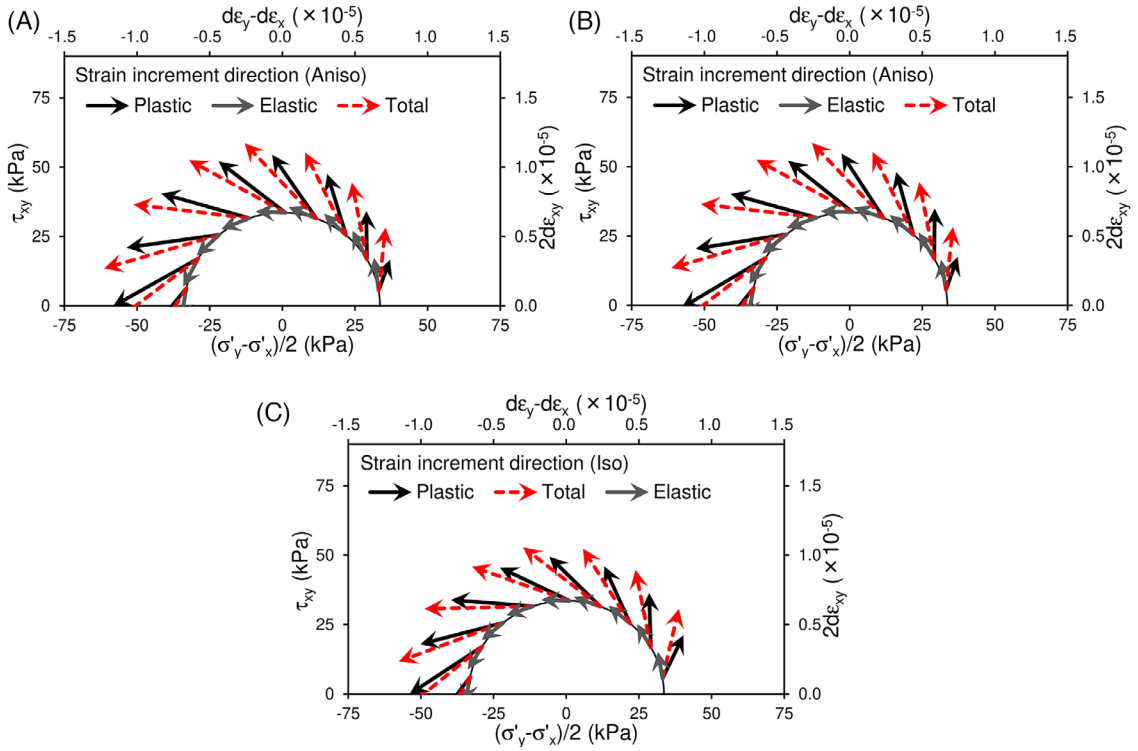

FIGURE 21 Magnitude and direction of simulated strain increments during the drained principal stress rotation tests for $\phi = 20°$: (A) with inherent anisotropy considering the anisotropic elastic shear modulus; (B) with inherent anisotropy considering the isotropic elastic shear modulus; (C) without inherent anisotropy

results presented in Figures 20B and C with the experimental counterparts in Figure 20A, it is evident that employing anisotropic parameters in the simulation improves the accuracy of prediction under drained PSR loading irrespective of the mobilized friction angle. The inherent anisotropy is also found to have a nonnegligible impact on not only the principal direction of simulated plastic strain increment but also its magnitude, as shown in Figure 21.

Next, the simulated responses in Figure 21 are organized in the relationship of $\alpha_{d\varepsilon^p}$, $\alpha_{d\varepsilon}$, and $\alpha_{d\varepsilon^e}$ with the applied α_σ and $\alpha_{d\sigma}$ in Figures 22 and 23; in these figures, $\alpha_{d\varepsilon^p}$ obtained from the experiments is also plotted. Figures 22A and 23A show that the simulated $\alpha_{d\varepsilon^e}$ does not always behave coaxial with $\alpha_{d\sigma}$, different from the coaxial response in Figures 22B and 23B, because of the anisotropic elastic shear modulus, G_m^{Iso}, in Equation (27). However, the simulated $\alpha_{d\varepsilon^p}$ shows almost the same response, for example, from a comparison of Figure 22A with 22B. In the early stage of PSR loading, the experimental $\alpha_{d\varepsilon^p}$ plots show more prominent noncoaxiality with α_σ; the constitutive model can better reproduce the measured response by taking into account the inherent anisotropy compared to the simulated responses in Figures 22C and 23C. After α_σ exceeds 15°, which corresponds to a counterclockwise angle of 30° relative to the x-axis (see Figure 19), the inherent anisotropy is found to decrease the degree of noncoaxiality similar to the trend of the experimental plots. Then, the degree of noncoaxiality in the experiment turns to an increase at around $\alpha_\sigma = 65°$ for $\phi = 20°$ (Figure 22) or remains approximately the same for $\phi = 30°$ (Figure 23); the strain space multiple mechanism model can accurately simulate such a complicated noncoaxial behavior by introducing the inherently anisotropic parameters.

Figure 24 compares the simulated developments of ε_z, ε_θ, and $\varepsilon_{z\theta}$ in response to α_σ with the corresponding experimental results for $\phi = 25°$, 30°, and 35°. For each mobilized friction angle, the anisotropic simulation is found to capture the experimental strain development than the isotropic simulation more reasonably. These results demonstrate that the effect of inherent anisotropy should be considered essential to accurately predict the behavior of soil subject to drained PSR loading.

Miura et al[1] also performed similar PSR tests on Toyoura sand with a relative density of 80% under a drained condition. In their tests, the soil samples were prepared using the multiple sieving pluviation method, which is considered to produce soil fabric (or inherent anisotropy) different from that produced by the dry-pluviation method. Figure 25 shows the four different PSR loadings applied in the experiment; after reaching the stress state of $R = (\sigma_1 - \sigma_3)/(\sigma_1 + \sigma_3) = 0.5$ along a proportional biaxial or simple shear loading path, α_σ was rotated counterclockwise while maintaining the stress

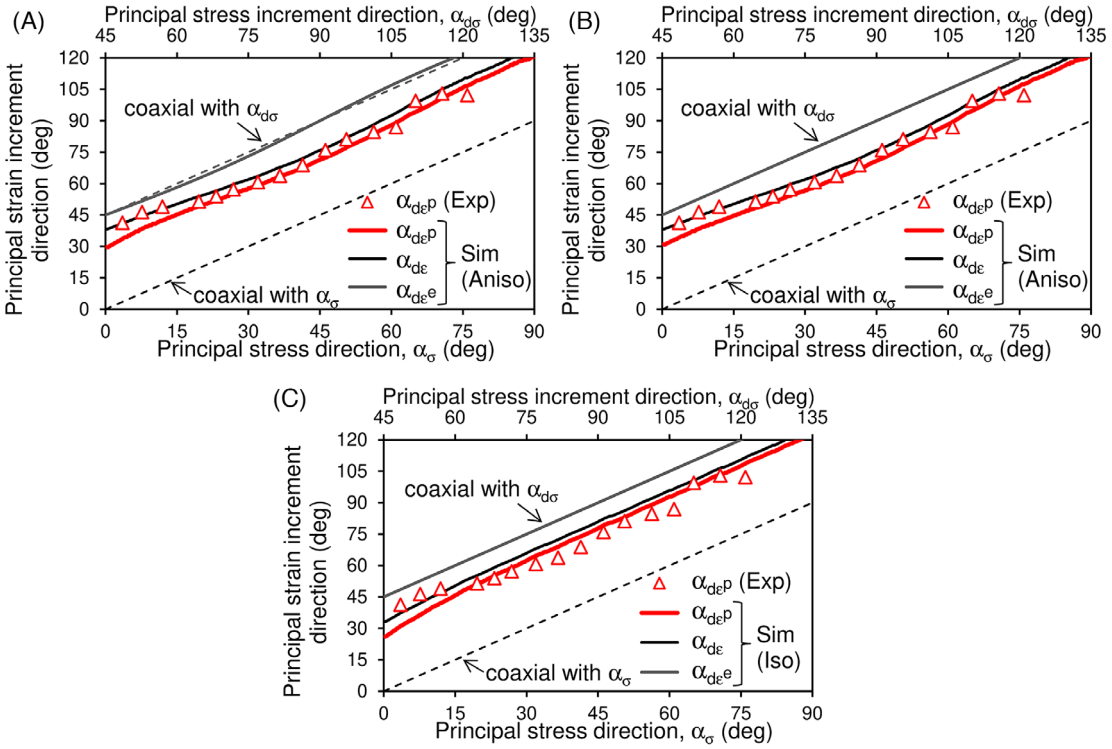

FIGURE 22 Comparison of simulated and measured principal plastic strain increment directions during the drained principal stress rotation tests for $\phi = 20°$ (Gutierrez et al[4]): (A) with inherent anisotropy considering the anisotropic elastic shear modulus; (B) with inherent anisotropy considering the isotropic elastic shear modulus; (C) without inherent anisotropy

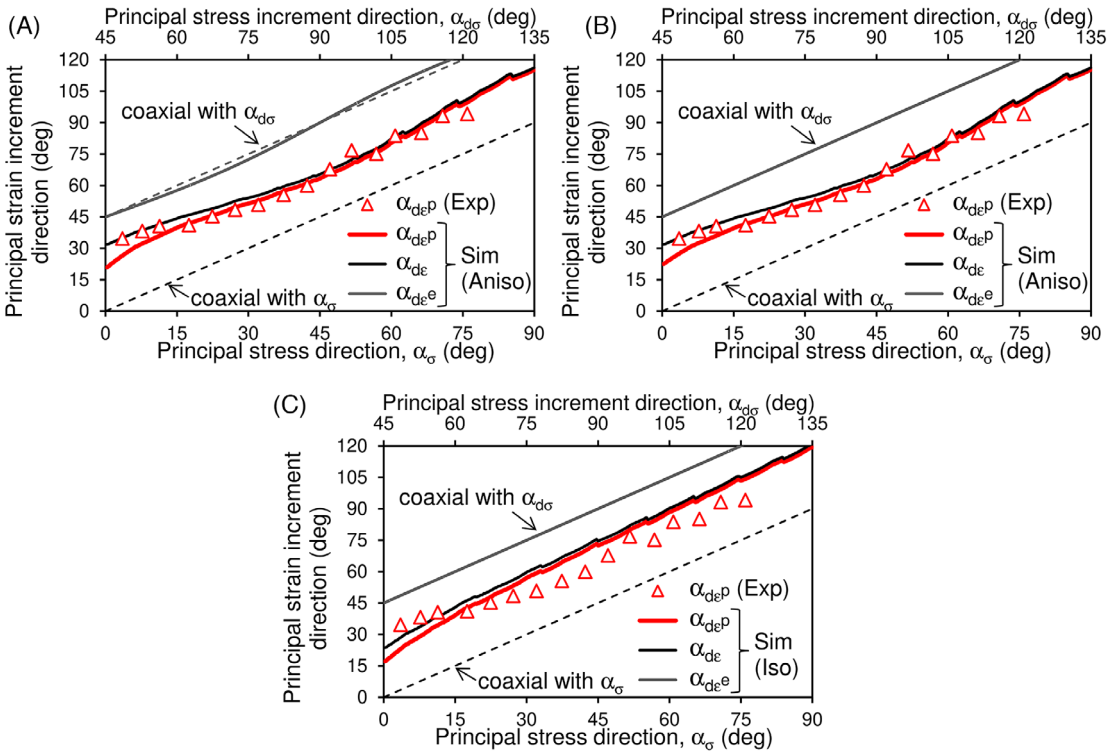

FIGURE 23 Comparison of simulated and measured principal plastic strain increment directions during the drained principal stress rotation tests for $\phi = 30°$ (Gutierrez et al[4]): (A) with inherent anisotropy considering the anisotropic elastic shear modulus; (B) with inherent anisotropy considering the isotropic elastic shear modulus; (C) without inherent anisotropy

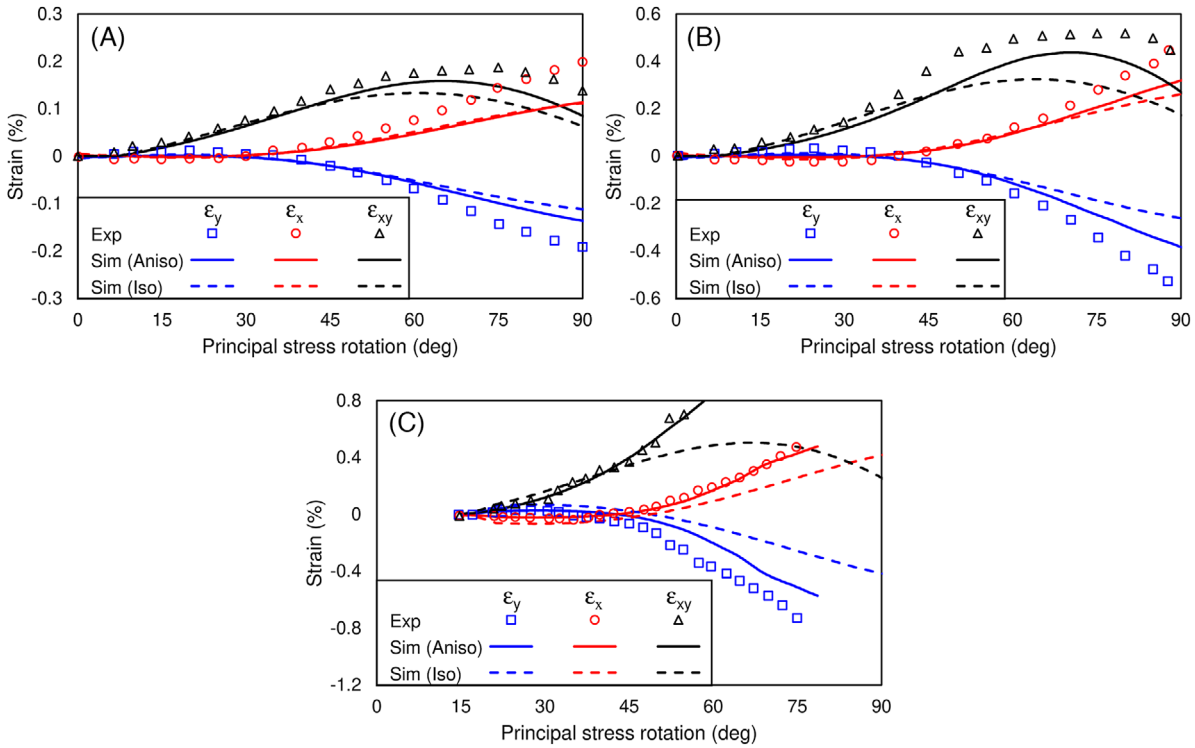

FIGURE 24 Comparison of simulated and measured strain developments during the drained principal stress rotation tests[4] for constant mobilized friction angles: (A) $\phi = 25°$; (B) $\phi = 30°$; (C) $\phi = 35°$

FIGURE 25 Deviator stress paths for the drained principal stress rotation tests performed by Miura et al[1]

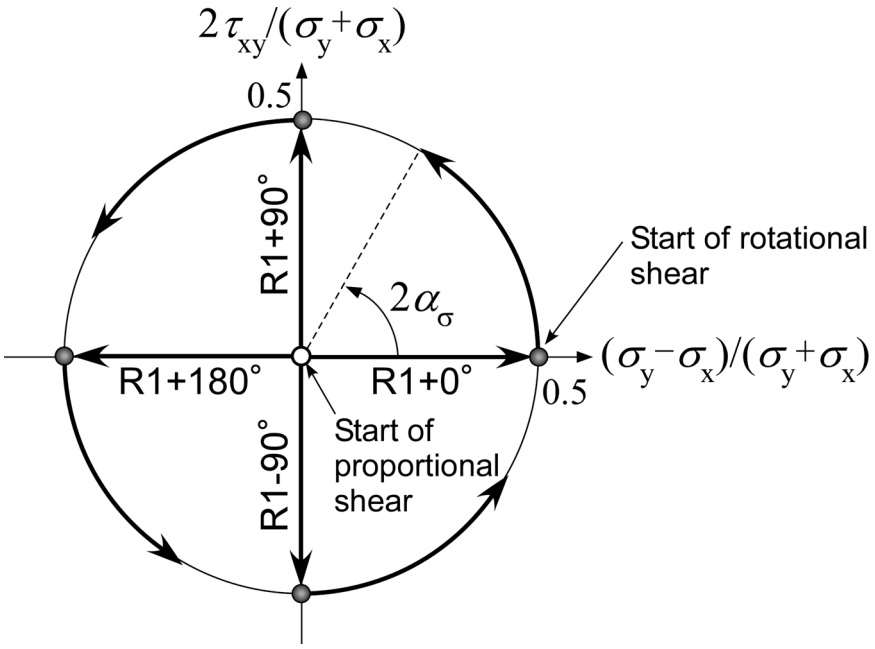

ratio constant. In the simulation, the model parameters in Table 4 were used; after the small-strain shear modulus was calculated from Equation (32), the strength and anisotropic parameters were calibrated.

Figure 26 illustrates simulated deviator strain paths under the four different loading paths along with the experimental results. As shown in Figure 26B, the simulated paths are found to have the property of rotational symmetry (eg, the R1-90° path becomes identical to the R1+180° path after a rotation of 90°) if the soil fabric is assumed isotropic; these results are entirely different from those of the experiment. However, the experimental strain paths are reasonably simulated by employing the anisotropic parameters, as seen in Figure 26A.

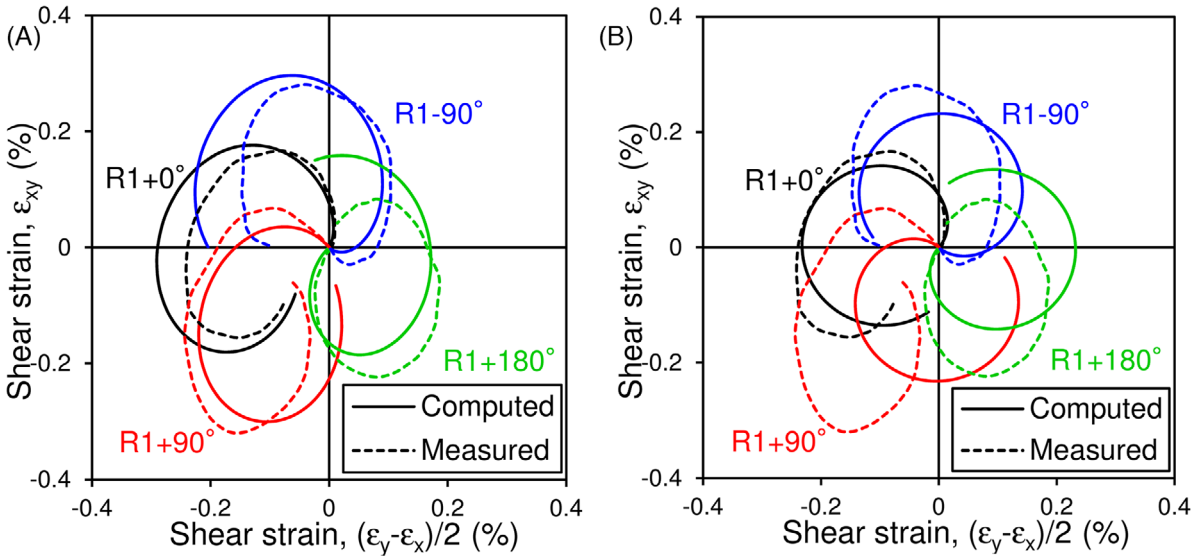

FIGURE 26 Deviator strain paths for the drained principal stress rotation tests with experimental results[1]: (A) simulation with inherent anisotropy; (B) simulation without inherent anisotropy

TABLE 4 Model parameters used for multiple-sieving-pluviated Toyoura sand with a relative density of 80%[1]

$K_{L/Ua}$ (kPa)	G_{ma} (kPa)	ϕ_f (°)	a_1	a_2	θ_0 (°)
237,059	90,902	47.0	0.18	0.15	90

(p_a = 98kPa).

Figure 27 illustrates the change in simulated $\alpha_{d\varepsilon^p}$, $\alpha_{d\varepsilon}$, and $\alpha_{d\varepsilon^e}$ during PSR loading in response to the applied α_σ and $\alpha_{d\sigma}$. In this figure, $\alpha_{d\varepsilon}$ in the experiments is also plotted as read from Figure 26 instead of measured $\alpha_{d\varepsilon^p}$; this is because Miura et al[1] did not derive the plastic strain increment, different from Gutierres et al[3] (see Figure 22). It is noted that $\alpha_{d\varepsilon^p}$ in Figure 27 was calculated by subtracting the anisotropic elastic strain increment obtained using Equation (27) from the simulated total strain increment. As shown in the figure, the simulated $\alpha_{d\varepsilon^e}$ with inherent anisotropy does not always behave coaxial with $\alpha_{d\sigma}$ because of the anisotropic elastic shear modulus, G_m^{Aniso}, different from the coaxial response without inherent anisotropy. Comparison of the simulated responses with inherent anisotropy under the four different PSR loadings reveals that the noncoaxiality between $\alpha_{d\varepsilon^e}$ and $\alpha_{d\sigma}$ looks different among the cases, but is identical only with a periodic difference; for example, the noncoaxial response of $\alpha_{d\varepsilon^e}$ with $\alpha_{d\sigma} = 180° - 225°$ does not change depending on the start position of rotational shear (eg, refer to Figures 27A and C).

In the absence of inherent anisotropy, the changes in $\alpha_{d\varepsilon^p}$ and $\alpha_{d\varepsilon}$ in response to α_σ (or $\alpha_{d\sigma}$) are found to be parallel to that in $\alpha_{d\varepsilon^e}$, except for the initial stage of PSR loading (see Figure 27B, for example); the simulated responses of $\alpha_{d\varepsilon}$ are somewhat different from the experimental plots. Meanwhile, the simulation considering the inherent anisotropy is capable of properly capturing the measured $\alpha_{d\varepsilon}$ changes in response to α_σ (or $\alpha_{d\sigma}$), for example, as shown in Figure 27A. Comparison of the simulated responses under the four different PSR loadings demonstrates that the noncoaxiality between $\alpha_{d\varepsilon^p}$ and α_σ does not change only with a phase difference (eg, 45° between the R1+0° and R1+90° paths) in the absence of inherent anisotropy, even though the start of rotational shear is different. In contrast, the noncoaxiality is found to become different depending on the start position, in addition to the phase difference, by taking into account the effect of inherent anisotropy.

Thus, it can be concluded that considering inherent anisotropy in numerical simulation is essential to accurately predict the response of soil subject to PSR loading, particularly when different proportional loading paths are used.

6 | CONCLUSIONS

This article discusses the capability of a strain space multiple mechanism model to reproduce complex responses of inherently anisotropic soils under various kinds of loading paths. The constitutive model has been expanded upon to account

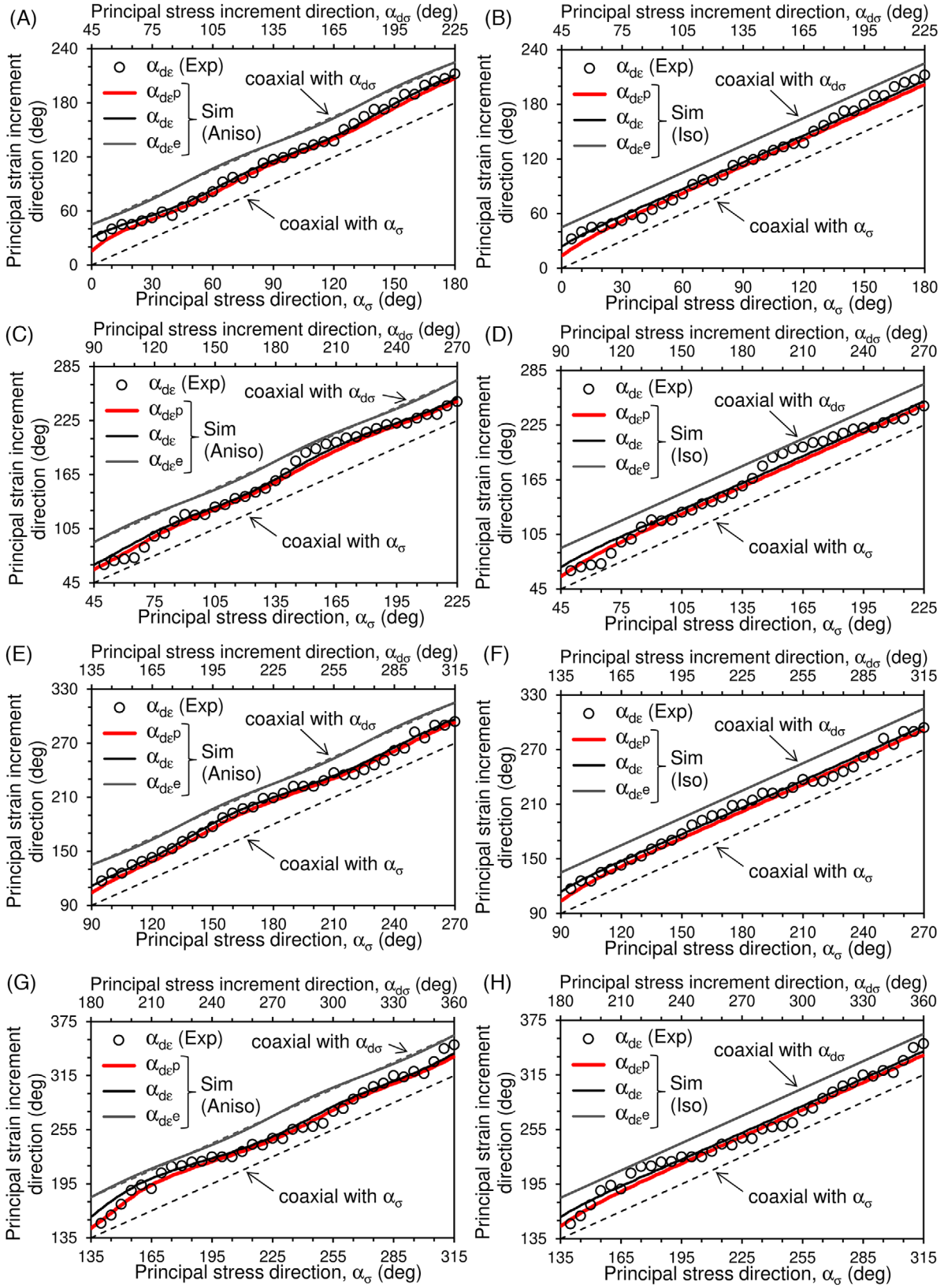

FIGURE 27 Comparison of simulated and measured principal (total) strain increment directions during the drained principal stress rotation tests[1]: (A), (B) R1+0° with or without inherent anisotropy; (C), (D) R1+90° with or without inherent anisotropy; (E), (F) R1+180° with or without inherent anisotropy; (G), (H) R1-90° with or without inherent anisotropy

for the effect of inherent anisotropy by incorporating a new function along with three additional parameters; two of these parameters, a_1 and a_2, control the degree of anisotropy whereas the third parameter, θ_0, represents the principal direction of inherent anisotropy. Laboratory experimental data regarding the complex anisotropic behavior of Toyoura sand under various loading paths is used to validate the constitutive model. Major conclusions are summarized as follows:

1. By introducing the anisotropic model parameters a_1 and a_2, the constitutive model is capable of representing an experimentally observed Mohr's circle (ie, shear failure envelop in the deviator stress plane) for inherently anisotropic granular materials, which has a distorted shape compared with the isotropic Mohr's circle.
2. The anisotropic elastic shear modulus depending on inherent anisotropy is essential to consider, particularly in the early stages of loading where the elastic behavior is dominant, for correctly determining the elastic and plastic components of a total strain increment in both experiments and simulations.
3. During undrained monotonic proportional loading with different principal strain directions, the noncoaxiality between the directions of principal strain and stress is found to become prominent when the effect of inherent anisotropy is considered. Furthermore, the soil behavior becomes completely coaxial irrespective of the inherent anisotropy's effect when the principal strain direction is parallel or perpendicular to the direction of the bedding plane.
4. During drained monotonic proportional loading with different principal stress directions, the anisotropic constitutive model is capable of simulating the experimental noncoaxial response from the early stage of loading almost to the failure surface. As the stress path approaches the failure surface, the direction of plastic strain increment gets closer to the coaxial state with the applied principal stress direction, but does not reach the perfect coaxiality simulated with no consideration for inherent anisotropy.
5. During drained monotonic nonproportional loading, the anisotropic constitutive model can reasonably capture the experimental response along a stress path where both the principal stress direction and the loading magnitude drastically change; the noncoaxiality between the directions of principal stress and plastic strain increment is more prominent in the early stage of loading and then gradually disappears as the stress path approaches the failure surface.
6. During the rotation of the principal stress axis with a constant deviator stress under a drained condition, employing the anisotropic parameters can improve the accuracy with which deviator strain paths and the development of strains are predicted. The noncoaxiality between the directions of principal stress and plastic strain increment is largely influenced by the inherent anisotropy; the start position of rotational shear also affects the noncoaxiality. Hence, it can be concluded that consideration of inherent anisotropy in numerical simulation is essential to accurately predict the response of soil subject to principal stress rotation loading.

This article investigated the noncoaxial behavior of inherently anisotropic soils, focusing on macroscopic stress/strain responses, through a comparison with laboratory test results. It is worth mentioning that the results of discrete element simulations may also be beneficial to validate the applicability of the proposed model from a microscopic perspective; this is because the virtual simple shear stress within this modeling framework is an intermediate quantity in the upscaling process from the microscopic level characterized by the contact distribution and interparticle contact forces.[35]

DATA AVAILABILITY STATEMENT

The data that support the findings of this study are available from the corresponding author (Kyohei Ueda) upon reasonable request.

ORCID

Kyohei Ueda https://orcid.org/0000-0001-6202-6431

REFERENCES

1. Miura K, Miura S, Toki S. Deformation behavior of anisotropic dense sand under principal stress axes rotations. *Soils Found*. 1986;26(1):36-52.
2. Pradel D, Ishihara K, Gutierrez M. Yielding and flow of sand under principal stress rotation. *Soils Found*. 1990;30(1):87-99.
3. Gutierrez M, Ishihara K, Towhata I. Flow theory for sand during rotation of principal stress direction. *Soils Found*. 1991;31(4):121-132.
4. Gutierrez M, Ishihara K, Towhata I. Model for the deformation of sand during rotation of principal stress directions. *Soils Found*. 1993;33(3):105-117.
5. Arthur JRF, Menzies BK. Inherent anisotropy in a sand. *Geotechnique*. 1972;22(1):115-128.
6. Oda M. Initial fabrics and their relation to mechanical properties of granular material. *Soils Found*. 1972;12(1):17-36.

7. Arthur JRF, Phillips AB. Homogeneous and layered sand in triaxial compression. *Géotechnique*. 1975;25(2):799-815.
8. Oda M, Koishikawa I. Anisotropic fabric of sands. Proceedings of the 9th International Conference on Soil Mechanics and Foundation Engineering (Tokyo). 1977;1:235-238.
9. Nakata Y, Hyodo M, Murata H, Yasufuku N. Flow deformation of sands subjected to principal stress rotation. *Soils Found*. 1998;38(2):115-128.
10. Uthayakumar M, Vaid YP. Static liquefaction of sands under multiaxial loading. *Canad Geotech J*. 1998;35(2):273-283.
11. Yoshimine M, Ishihara K, Vargas W. Effects of principal stress direction and intermediate principal stress on undrained shear behavior of sand. *Soils Found*. 1998;38(3):179-188.
12. Lade PV, Kirkgard MM. Effects of stress rotation and changes of b-values on cross-anisotropic behavior of natural, K0-consolidated soft clay. *Soils Found*. 2000;40(6):93-105.
13. Dafalias YF, Papadimitriou AG, Li XS. Sand plasticity model accounting for inherent fabric anisotropy. *J Eng Mech(ASCE)*. 2004;130(11):1319-1333.
14. Li XS, Dafalias YF. A constitutive framework for anisotropic sand including non-proportional loading. *Geotechnique*. 2004;54(1):41-55.
15. Tsutsumi S, Hashiguchi K. General non-proportional loading behavior of soils. *Int J Plast*. 2005;21(10):1941-1969.
16. Li XS, Dafalias YF. Anisotropic critical state theory: the role of fabric. *J Eng Mech*. 2012;138(3):263-275.
17. Gao Z, Zhao J. Constitutive modeling of artificially cemented sand by considering fabric anisotropy. *Comput Geotech*. 2012;41:57-69.
18. Yang YM, Yu HS. A kinematic hardening soil model considering the principal stress rotation. *Int J Numer Anal Methods Geomech*. 2013;37(13):2106-2134.
19. Gao ZW, Zhao JD, Li S, Dafalias YF. A critical state sand plasticity model accounting for fabric evolution. *Int J Numer Anal Methods Geomech*. 2014;38(40):370-390.
20. Zhao J, Gao Z. Unified anisotropic elastoplastic model for sand. *J Eng Mech*. 2016;142(1):04015056.
21. Towhata I, Ishihara K. Modelling soil behaviour under principal stress axes rotation. *In Proceedings of the 5th International Conference on Numerical Methods in Geomechanics Balkema: Nagoya*. 1985:523-530.
22. Iai S, Matsunaga Y, Kameoka T. Strain space plasticity model for cyclic mobility. *Soils Found*. 1992;32(2):1-15.
23. Iai S, Ozutsumi O. Yield and cyclic behaviour of a strain space multiple mechanism model for granular materials. *Int J Numer Anal Methods Geomech*. 2005;29(4):417-442.
24. Iai S, Tobita T, Ozutsumi O, Ueda K. Dilatancy of granular materials in a strain space multiple mechanism model. *Int J Numer Anal Methods Geomech*. 2011;35(3):360-392.
25. Ueda K, Iai S. Constitutive modeling of inherent anisotropy in a strain space multiple mechanism model for granular materials. *Int J Numer Anal Methods Geomech*. 2019;43(3):708-737.
26. Jiang MJ, Harris D, Yu HS. Kinematic models for non-coaxial granular materials. Part I: theory. *Int J Numer Anal Methods Geomech*. 2005;29(7):643-661.
27. Jiang MJ, Harris D, Yu HS. Kinematic models for non-coaxial granular materials. Part II: evaluation. *Int J Numer Anal Methods Geomech*. 2005;29(7):663-689.
28. Thornton C, Zhang L. A numerical examination of shear banding and simple shear non-coaxial flow rules. *Philos Mag*. 2006;86(21-22):3425-3452.
29. Li X, Yu HS. Numerical investigation of granular material behaviour under rotational shear. *Geotechnique*. 2010;60(5):381-394.
30. Ai J, Langston PA, Yu HS. Discrete element modelling of material non-coaxiality in simple shear flows. *Int J Numer Anal Methods Geomech*. 2014;38(6):615-635.
31. Tong ZX, Fu P, Dafalias YF, Yao YP. Discrete element method analysis of non-coaxial flow under rotational shear. *Int J Numer Anal Methods Geomech*. 2014;38(14):1519-1540.
32. Milton GW. *The Theory of Composites*. Cambridge University Press; 2002. pp. 51-52, and 105.
33. Boresi AP, Schmidt RJ, Sidebottom OM. *Advanced Mechanics of Materials*. 6th ed. Wiley; 2009. pp. 93-95.
34. Iai S, Tobita T, Ozutsumi O. Induced fabric under cyclic and rotational loads in a strain space multiple mechanism model for granular materials. *Int J Numer Anal Methods Geomech*. 2013;37(2):150-180.
35. Iai S, Tobita T, Ozutsumi O. Evolution of induced fabric in a strain space multiple mechanism model for granular materials. *Int J Numer Anal Methods Geomech*. 2013;37(10):1326-1336.
36. Christoffersen J, Mehrabadi MM. Nemat-Nasser S. A micromechanical description of granular material behavior. *J Appl Mech*. 1981;48(2):339-344.
37. Mehrabadi MM, Nemat-Nasser S, Oda M. On statistical description of stress and fabric in granular materials. *Int J Numer Anal Methods Geomech*. 1982;6(1):95-108.
38. Rothenburg L, Bathurst RJ. Analytical study of induced anisotropy in idealized granular materials. *Geotechnique*. 1989;39(4):601-614.
39. Iai S, Ueda K. Energy-less strain in granular materials - micromechanical background and modeling. *Soils Found*. 2016;56(3):391-398.
40. Hardin BO, Drnevich VP. Shear modulus and damping in soils: design equation and curves. *J Soil Mech Found Div(ASCE)*. 1972;98(SM7):667-692.
41. Ishihara K. *Soil Behaviour in Earthquake Geotechnics*. Oxford University Press; 1996. pp. 87-92.
42. Arthur JRF, Chua KS, Dunstan T, RdC JI. Principal stress rotation: a missing parameter. *J Geotech Eng Div*. 1980;106(GT4):419-433.

How to cite this article: Ueda K, Iai S. Noncoaxiality considering inherent anisotropy under various loading paths in a strain space multiple mechanism model for granular materials. *Int J Numer Anal Methods Geomech*. 2021;45:815–842. https://doi.org/10.1002/nag.3183

APPENDIX A

The strain space multiple mechanism model accounting for inherent anisotropy is originally derived in consideration of material nonlinearity as shown in Equation (23). Here, the constitutive equation is rewritten by ignoring the material nonlinearity to compare with the stress-strain relationship below for orthotropic linear elastic materials.[32,33]

$$\begin{Bmatrix} \varepsilon_x^e \\ \varepsilon_y^e \\ \gamma_{xy}^e \end{Bmatrix} = \begin{bmatrix} \frac{1}{E_x} - \frac{\nu_{zx}^2}{E_z} & -\frac{\nu_{yx}}{E_y} - \frac{\nu_{zx}\nu_{zy}}{E_z} & 0 \\ -\frac{\nu_{xy}}{E_x} - \frac{\nu_{zx}\nu_{zy}}{E_z} & \frac{1}{E_y} - \frac{\nu_{zy}^2}{E_z} & 0 \\ 0 & 0 & \frac{1}{G_{xy}} \end{bmatrix} \begin{Bmatrix} \sigma_x \\ \sigma_y \\ \tau_{xy} \end{Bmatrix}, \tag{33}$$

where E_i is the Young's modulus of the material in direction $i = x, y, z$, and ν_{ij} is the Poisson's ratio representing the ratio of a transverse strain to the applied strain in uniaxial tension or compression; for example, $\nu_{xy} = -\varepsilon_y^e/\varepsilon_x^e$ for uniaxial tension or compression in the x-direction. By applying the symmetric properties $\nu_{yz}E_z = \nu_{zy}E_y$ and $\nu_{xz}E_z = \nu_{zx}E_x$ to the above equation, the normal strain difference, $\varepsilon_y^e - \varepsilon_x^e$, and shear strain, γ_{xy}^e, are given by

$$\varepsilon_y^e - \varepsilon_x^e = A\left\{\left(1 + \frac{B}{A}\right)\sigma_y - \left(1 - \frac{B}{A}\right)\sigma_x\right\}, \tag{34}$$

$$\gamma_{xy}^e = \frac{1}{G_{xy}}\tau_{xy}, \tag{35}$$

where

$$A = \frac{1}{2}\left\{\frac{1+\nu_{xy}}{E_x} + \frac{1+\nu_{yx}}{E_y} - \frac{\left(\nu_{zx} - \nu_{zy}\right)^2}{E_z}\right\}, \tag{36}$$

$$B = \frac{1}{2}\left(\frac{1-\nu_{yz}\nu_{zy}}{E_y} - \frac{1-\nu_{xz}\nu_{zx}}{E_x}\right). \tag{37}$$

Since the nonlinear hysteretic function in Equation (20) can be simplified into a linear relationship as $q_{\mathrm{Iso}} = (q_{\mathrm{v}}/\gamma_{\mathrm{v}})\gamma^{\mathrm{e}}$, where γ^{e} is the elastic virtual simple shear strain, the strain space multiple mechanism model is written as follows:

$$\boldsymbol{\sigma} = -p\mathbf{I} + \int_0^{\pi} q\,\langle \mathbf{t} \otimes \mathbf{n} \rangle\, \mathrm{d}\omega, \tag{38}$$

where

$$p = -K\varepsilon^{\mathrm{e}} = -K\left(\varepsilon_{\mathrm{x}}^{\mathrm{e}} + \varepsilon_{\mathrm{y}}^{\mathrm{e}}\right), \tag{39}$$

$$q = \{1 + a_2 \cos 2(\omega - \omega_0)\}\frac{q_{\mathrm{v}}}{\gamma_{\mathrm{v}}}\gamma^{\mathrm{e}} - \frac{1}{\pi}a_1 \cos(\omega - \omega_0)\, p', \tag{40}$$

$$\gamma^{\mathrm{e}} = \left(\varepsilon_{\mathrm{x}}^{\mathrm{e}} - \varepsilon_{\mathrm{y}}^{\mathrm{e}}\right)\cos\omega + \gamma_{\mathrm{xy}}^{\mathrm{e}}\sin\omega. \tag{41}$$

In Equation (38), the effective stress tensor, $\boldsymbol{\sigma}'$, is replaced with the total stress tensor, $\boldsymbol{\sigma}$, because there is no need to distinguish between $\boldsymbol{\sigma}'$ and $\boldsymbol{\sigma}$ for the modeling of elastic materials. The relationship between the isotropic stress and volumetric strain in Equation (39) is also assumed to be linear using the elastic bulk modulus, K. By assuming the horizontal bedding plane (ie, $\theta_0 = \pi/2$) corresponding to orthotropic linear elastic materials, Equation (38) can be rewritten using Equation (29) as follows:

$$\boldsymbol{\sigma} = K\varepsilon^{\mathrm{e}}\begin{bmatrix} 1+\frac{1}{2}a_1 & 0 \\ 0 & 1-\frac{1}{2}a_1 \end{bmatrix} + G_{\mathrm{m}}^{\mathrm{Iso}}\begin{bmatrix} \left(1+\frac{1}{2}a_2\right)\left(\varepsilon_{\mathrm{x}}^{\mathrm{e}} - \varepsilon_{\mathrm{y}}^{\mathrm{e}}\right) & \left(1-\frac{1}{2}a_2\right)\gamma_{\mathrm{xy}}^{\mathrm{e}} \\ \left(1-\frac{1}{2}a_2\right)\gamma_{\mathrm{xy}}^{\mathrm{e}} & -\left(1+\frac{1}{2}a_2\right)\left(\varepsilon_{\mathrm{x}}^{\mathrm{e}} - \varepsilon_{\mathrm{y}}^{\mathrm{e}}\right) \end{bmatrix}. \tag{42}$$

The above equation in tensor form can be rewritten to vector-matrix form as

$$\begin{Bmatrix} \sigma_x \\ \sigma_y \\ \tau_{xy} \end{Bmatrix} = \begin{bmatrix} \left(1+\frac{a_1}{2}\right)K + \left(1+\frac{a_2}{2}\right)G_{\mathrm{m}}^{\mathrm{Iso}} & \left(1+\frac{a_1}{2}\right)K - \left(1+\frac{a_2}{2}\right)G_{\mathrm{m}}^{\mathrm{Iso}} & 0 \\ \left(1-\frac{a_1}{2}\right)K - \left(1+\frac{a_2}{2}\right)G_{\mathrm{m}}^{\mathrm{Iso}} & \left(1-\frac{a_1}{2}\right)K + \left(1+\frac{a_2}{2}\right)G_{\mathrm{m}}^{\mathrm{Iso}} & 0 \\ 0 & 0 & \left(1-\frac{1}{2}a_2\right)G_{\mathrm{m}}^{\mathrm{Iso}} \end{bmatrix}\begin{Bmatrix} \varepsilon_x^e \\ \varepsilon_y^e \\ \gamma_{xy}^e \end{Bmatrix}. \tag{43}$$

Considering the inverse of the stiffness matrix, the normal strain difference, $\varepsilon_y^e - \varepsilon_x^e$, and shear strain, γ_{xy}^e, are given in the (elastic) strain space multiple mechanism model accounting for inherent anisotropy as follows:

$$\varepsilon_y^e - \varepsilon_x^e = \frac{1}{(2+a_2)G_m^{Iso}}\left\{\left(1+\frac{a_1}{2}\right)\sigma_y - \left(1-\frac{a_1}{2}\right)\sigma_x\right\}, \tag{44}$$

$$\gamma_{xy}^e = \frac{1}{\left(1-\frac{1}{2}a_2\right)G_m^{Iso}}\tau_{xy}. \tag{45}$$

When the parameter a_2 is equal to zero, the relationship between the shear stress and shear strain does not depend on the inherent anisotropy; however, a nonzero normal strain difference, $\varepsilon_y^e - \varepsilon_x^e$, occurs due to $\sigma_x + \sigma_y$ even under the condition of $\sigma_y - \sigma_x = 0$ as shown in Equation (44). Hence, the principal direction of the elastic strain, α_{ε^e}, becomes noncoaxial with the principal stress direction, α_σ, as the Mohr's strain circle in Figure 2C demonstrates. Meanwhile, when the parameter a_1 is equal to zero, the normal strain difference does not depend on $\sigma_x + \sigma_y$, but both the strain difference and shear strain are affected by the parameter a_2. Thus, the Mohr's strain circle is horizontally and vertically distorted by the inherent anisotropy as shown in Figure 2D, resulting in the noncoaxiality between α_{ε^e} and α_σ.

Comparison of Equations (44) and (45) with Equations (34) and (35) demonstrates that the strain space multiple mechanism model accounting for inherent anisotropy given by Equation (23) is equivalent to the orthotropic linear elastic model given by Equation (33) in the elastic domain; the parameters of both models are related as follows:

$$G_m^{Iso} = \frac{1+2AG_{xy}}{4A}, \tag{46}$$

$$a_1 = \frac{2B}{A}, \tag{47}$$

$$a_2 = \frac{2\left(1-2AG_{xy}\right)}{1+2AG_{xy}}. \tag{48}$$

Also, the proposed model can be regarded as a natural extension of the existing model for orthotropic linear elastic materials to the nonlinear domain.